An Optimized Approach for Methanol Production from CO_2 by a Novel Magnetic MIL-101(Fe)-NH_2-GO Photocatalyst via Response Surface Methodology

Mohammad Shahryari Mazraeh Shahi[1], Leila Vafajoo[1, 2*], Mohammad Kazemeini[3*]

[1]Chemical and Polymer Engineering Department, ST. C., Islamic Azad University, Tehran, Iran

[2]Nanotechnology Research Center, ST. C., Islamic Azad University, Tehran, Iran

[3]Department of Chemical and Petroleum Engineering, Sharif University of Technology, P.O. Box b11365-94655, Tehran, Iran

*: Corresponding Authors emails: vafajoo@iau.ac.ir and kazemini@sharif.edu

Abstract

Global warming, fueled by rising greenhouse gas concentrations in the atmosphere, stands as a significant environmental challenge in the 21st century. The mounting concerns have sparked a surge in research efforts aimed at harnessing CO_2 conversion into valuable compounds. This investigation delves into the synthesis and characterization MI-101(Fe)-NH_2-GO-Fe_3O_4 photocatalyst, particularly focusing on the impact of NH_2 surface modification on MIL-101(Fe) in methanol production enhancement. The results notably indicate an enhancement in the performance of the photocatalyst following the surface modification of MIL-101(Fe). Notably, MIL-101(Fe)-NH_2-GO with 10% Fe_3O_4 photocatalyst exhibits the narrowest band gap at 1.68 eV, indicating superiority in catalytic activity. The study further establishes a p-n heterojunction in MIL-101(Fe)-NH_2-GO with 10% Fe_3O_4 photocatalyst, signifying advanced catalytic properties. An experimental framework utilizing design of experiment was implemented to investigate the influence of various factors, including time, catalyst dosage, weight percentage of Fe_3O_4, and pH, on operational parameters, with the aim of optimizing these variables. The study achieved methanol production of 2978.25 mg/L under optimal conditions, using 0.46 g of MIL-101(Fe)-NH_2-GO with 7.82% Fe_3O_4 photocatalyst in 107 min at pH 5. Further examination of the process through GC-MS identified methanol, formamide, and formaldehyde as the main products.

Keywords: CO_2 capture; MIL-101(Fe)-NH_2-GO; Optimization; Methanol; Fuel

1. Introduction

The 21st century is the era of severe concern of the world community about the excessive emission of CO_2 gas [1, 2]. The development and progress of the global industry has led to a greater demand for energy and the subsequent use of fossil fuels as a source of energy supply; Therefore, in addition to the environmental challenges, the lack of energy should also be considered. Achieving a comprehensive solution is a controversial point in many researches. One of the relatively comprehensive solutions that has the ability to supply fuel and reduce CO_2 at the same time is to use solar energy to convert [3-5]. Therefore, simultaneously removing CO_2 and turning it into a value-added product is a very ideal point. Currently, due to the lack of a fully efficient catalyst, few CO_2 adsorption and conversion processes are used on a large industrial scale; Therefore, researchers are trying to invent suitable heterogeneous catalysts [6]. Metal-organic frameworks (MOFs) have garnered significant attention from researchers in recent years due to their wide range of modifiable structures and high porosity, positioning them as a relatively novel category of catalysts. This research primarily focuses on exploring the properties and applications of MOFs in catalysis [7-12]. MOFs have found extensive application in various catalytic processes, including the degradation of pollutants, the production of hydrogen, and the reduction of CO2. As such, their photocatalytic activity can be increased by modifying ligands, using sensitizers, and connecting with semiconductors [13, 14]. MOFs represent a fascinating category of porous crystalline hybrid structures characterized by their infinite regular frameworks comprising metal ions or clusters at the core and organic binders serving as bridges. The diversity within these structures is evident in the variations observed in the links and branches, which can differ in terms of size, shape, composition, geometry, and branching patterns [15]. The unique properties of MOFs facilitate the development of a wide range of crystalline porous materials, highlighting their adaptability and potential utility across diverse applications [16].

A group of MOFs utilized for the absorption of CO_2 gas falls under the category of Materials of Institute Lavoisier (MIL) [17, 18]. This particular class of MOFs was designed using trivalent metals as the central metal ions and carboxylic acid linkers. MILs have garnered significant attention for their exceptional gas absorption and separation capabilities, stemming from their remarkable porosity, expansive cross-sectional area, and amenability to functionalization [19]. MIL-101 (Fe) stands out as a well-researched iron-based metal-organic framework, featuring a core composed of iron ions and terephthalic acid ligands [20]. MIL-101 (Fe) is characterized by several remarkable features, including an exceptionally high specific surface area, substantial pore dimensions, and outstanding stability under both chemical and thermal conditions. The framework also exhibits unsaturated Lewis acid sites within its structure, imparting favorable characteristics for interactions with water molecules[21]. Owing to its distinct physicochemical properties and structural features, MIL-101 (Fe) finds wide-ranging applications in aqueous-phase absorption, storage, gas separation, and catalysis processes [22, 23]. Consequently, it finds utility across various domains such as electrocatalysis [24], photocatalysis [21], adsorption [25], membranes [25], sensor technology [26], drug delivery systems [27], and other crucial fields of study. Through a comprehensive examination of these compounds, their utilization can be extended to catalytic reactions, gas separation processes, and CO_2 absorption mechanisms. It is imperative to note that the polyamine chains within these frameworks should be kept relatively short, with the predominant basic groups being Lewis amines, responsible for the heightened absorption efficiency facilitated by the presence of these sites and nano-sized channels [27]. By amination MILs, they can be used in photocatalytic processes, gas separation and CO_2 adsorption. Of course, due to the narrow cavities of these structures, the polyamine chain should be short. Studies have shown that the absorption sites are the basic groups of Lewis amines and high absorption is due to these sites and nano-sized channels [27-29].

Natural graphene is a quasi-metal or a semiconductor with zero energy gap and also has very high electron mobility at room temperature [18]. On the contrary, the broad dimension of the graphene oxide (GO) strip serves as a substantial electron acceptor species, thereby enhancing the efficiency of charge transfer processes within the material [30]. This phenomenon leads to a decrease in the recombination rate of electrons and holes, and as a result, the overall efficiency of the photocatalytic system increases [31]. The physical and chemical properties of magnetic nanoparticles make them highly efficient tools in chemical and industrial fields. These unique properties stem from their nanoscale dimensions, which imbue them with enhanced reactivity and responsiveness to external stimuli [32]. Furthermore, magnetic nanoparticles can be effectively dispersed in aqueous solutions or organic solvents through the utilization of surfactants, thereby facilitating the creation of magnetic liquids with diverse functionalities and potential uses in various fields [33]. Magnetite Fe_3O_4 garners significant interest because of its distinctive and uncommon characteristics, along with its inherent utility in diverse fields [34]. Magnetite Fe_3O_4 exhibits a black color and demonstrates ferromagnetic characteristics at a macroscopic scale. The magnetic properties of magnetite nanoparticles have garnered significant interest, leading to a wide array of applications including imaging, soft magnetic materials, photocatalysts, among others [35-37].

The main objective of this research is to conduct a comprehensive analysis of how the amination of MIL influences the photocatalytic conversion of CO_2 into fuel. This research will delve into the intricate details of how amination alters the catalytic properties of MIL, shedding light on its potential for enhancing the efficiency and selectivity of the CO_2 conversion process. Furthermore, the investigation will involve meticulous scrutiny and fine-tuning of the operational parameters using the RSM to achieve optimal conditions for the photocatalytic reaction.

2. Experimental details

2.1 Materials

Iron (II) chloride ($FeCl_2$), Iron (III) chloride ($FeCl_3$), N,N-Dimethylformamide (DMF) (C_3H_7NO 99.8%), 2-Aminoterephthalic acid (NH_2-H_2 bdc) ($C_8H_7NO_4$) , graphite, sodium nitrate ($NaNO_3$), Potassium permanganate ($KMnO_4$ 99%), H_2O_2 and sulfuric acid (H_2SO_4 98%) were acquired from Merck.

2.2. Method

2.2.1 Synthesis of MIL-101(Fe)-NH_2

The preparation of MIL-101(Fe)-NH_2 initially commenced with the utilization of a hydrothermal approach. Initially, 1.24 mmol of NH2-H2 bdc was combined with 7.5 mL of DMF and placed on a magnetic stirrer for 30 minutes to produce a uniform solution referred to as solution 1. Following this, 2.5 mmol of $FeCl_3.6H_2O$ was mixed with 7.5 mL of DMF and stirred for 30 minutes to yield solution 2. Subsequently, solution 1 was gradually added to solution 2 in a dropwise manner and agitated for a period of one hour to guarantee thorough integration. The resultant mixture was subsequently transferred to an autoclave system and exposed to an oven setting maintained at 110°C for a duration of 24 hours to facilitate the formation of the desired product. The resulting orange-hued precipitate obtained was meticulously washed four times with DMF solvent at a temperature of 70 °C to remove any impurities or unreacted reagents. The washed precipitate was dried at 80°C for 2 hours.

2.2.2 Synthesis of GO-Fe_3O_4

A total of 0.05, 0.1, and 0.2 g of Fe_3O_4 were amalgamated with 1 g of GO in a volume of 25 mL of deionized water, subjected to agitation for a duration of 6 h utilizing a mechanical shaker, subsequently followed by magnetic separation through centrifugation and the thermal drying of the resultant composite particles at a temperature of 80 ^{o}C in a controlled oven environment.

2.2.3 Synthesis of MIL-101(Fe)-NH_2-GO-Fe_3O_4

0.1, 0.125, and 0.2 g of Go-Fe_3O_4 along with 1 g of MIL-101 (Fe)-NH_2 were combined in a 20 mL aqueous solution and agitated using a shaker for a duration of 4 hours. Subsequently, the resultant particles were isolated by means of a centrifugation process, followed by subjecting them to a final drying stage conducted within an oven maintained at a temperature of 60 ^oC. The utilization of such methodological steps ensures the successful synthesis and preparation of the desired composite materials with tailored properties for specific applications in various fields.

2.2.4 Photocatalytic conversion of CO_2 into fuel

In this research, a discontinuous photocatalytic reactor made of quartz was designed and built, and the performance of the synthesized catalysts with the highest specific level of selectivity and photocatalytic conversion of CO_2 to methanol in the mentioned reactor was investigated. Also, the effect of Fe_3O_4 weight percentage, photocatalyst mass, pH, time and modification of MIL-101(Fe) surface by NH_2 in fuel production was studied and investigated. In this manner, the photocatalysts that were synthesized, in conjunction with 50 mL of distilled water, were subjected to UVA light emanating from a source with a power of 15 watts for varying durations. The objective was to validate the generation of methanol through an examination of the samples utilizing Gas Chromatography with Flame Ionization Detection (GC-FID) and Gas Chromatography-Mass Spectrometry (GC-MS) subsequent to the completion of the photocatalytic procedure. The column used in this study was non-polar and HP1. This experimental approach was crucial in determining the efficacy of the photocatalysts in facilitating the conversion of methanol under the influence of UVA light.

2.2.5 Design of Experiment

Response surface methodology (RSM) encompasses a suite of statistical techniques that are adeptly utilized in the optimization of processes where the desired results are concurrently affected by numerous variables [38, 39]. By employing this sophisticated statistical approach, the necessity for conducting numerous experiments is mitigated significantly, leading to a more efficient and cost-effective experimental design. Furthermore, RSM enables the estimation of all coefficients within the quadratic regression model and facilitates the assessment of the interplay between various factors, thereby providing valuable insights for process optimization and improvement [40, 41]. In the present study, the RSM based on BBD was used. Additionally, this approach facilitated the optimization of combinations through the use of Design Expert 11 software. The effects of multiple variables, such as duration, photocatalyst mass, percentage of Fe_3O_4 by weight, and pH levels, were thoroughly analyzed across three separate tiers to gain a holistic understanding of their impact on the aggregate results (Table 1). By employing this methodological framework, the researchers sought to gain valuable insights into the intricate interplay between the specified variables and the responses generated, thereby facilitating the optimization of the experimental conditions for enhanced efficacy and performance. The general response surface equation is a mathematical representation that encapsulates the relationship between multiple input variables and an output response in a comprehensive manner, allowing for the exploration and analysis of complex systems through a structured and systematic approach.

$$Y = \beta_0 + \sum_{j=1}^{k} \beta_j X_j + \sum_{j=1}^{k} \beta_{jj} X_j^2 + \sum_{i} \sum_{<j=2}^{k} \beta_{ij} X_i X_j + e_i \qquad (1)$$

Y denotes the expected outcome (Methanol synthesis (mg/L)), wherein Xi and Xj represent independent variables expressed in coded formats, β0 indicates the constant term, and βi, βjj, and β_{ij} refer to the coefficients associated with linear, quadratic, and interaction effects, respectively, with k denoting the number of variables and e_i symbolizing the error in the model.

3 Results and discussion

3.1 Characterization

The XRD pattern identified for MIL-101(Fe)-NH_2 at 2Θ angles of 9.35, 11.9, 18.65, 21.95, 24.24, 25.95, 33.35, and 36.0 aligns with the established reference standard, thereby furnishing compelling evidence for the effective synthesis of MIL-101(Fe)-NH_2 with an exceptionally high degree of purity. XRD patterns of MIL-101(Fe)-NH_2-GO-Fe_3O_4 5%, MIL-101(Fe)-NH_2-GO-Fe_3O_4 10%, MIL-101(Fe)-NH_2-GO-Fe_3O_4 20% at 2Θ 9.35, 11.9, 18.65, 21.95, related to MIL-101(Fe)-NH_2 and at 2Θ 30.0, 35.5, 43.1, 53.6, 57.2, 62.5^o corresponding to Miller plates (220), (311), (400), (422), (511) respectively and (440) correspond to Fe_3O_4 (Figure 1). Also, All diffraction peaks exhibit a strong correspondence with the typical characteristic diffractions associated with the Fe_3O_4 nanoparticles inverse spinel configuration (JCPDS card no. 89-0691).

The results of FTIR for MIL-101 (Fe)-NH_2 are illustrated in Figure 2. The peak detected at approximately 3400 cm^{-1} is attributed to the NH_2 functional group. Concurrently, the vibrational bands observed around 2900 cm-1 are associated with the methylene groups within the NH_2-H_2BDC benzene ring. The spectral peaks observed within the interval of 1300-1700 cm^{-1} are associated with C-O vibrational modes. Furthermore, the stretching frequency corresponding to Fe-O is identified within the range of 541 cm^{-1}. All these results indicated that the coordination bond with NH_2-H_2BDC molecular Fe^{2+} ions is with the carbonyl group (C=O), not the amine group (NH_2). FTIR spectra for MIL101-(Fe) NH_2-GO-Fe_3O_4 5%, MIL-101 (Fe)-NH_2-GO-Fe_3O_4 10%, MIL-101 (Fe) -NH_2-GO-Fe_3O_4 20% catalysts are shown in Figure 2. The elastic band observable at 550 cm^{-1} is associated with the Fe-O stretching vibration found in Fe_3O_4, a significant compound in materials science. This particular vibrational mode offers significant understanding regarding the bonding attributes and structural characteristics of the Fe_3O_4 material. Furthermore, the stretching band located at 750 cm^{-1} is specifically attributed to the out-of-plane C-H bending vibration occurring in the H_2BDC benzene ring within the framework of MIL-101(Fe), a metal-organic framework known for its diverse applications in catalysis and gas storage. The bands observed in the range of 1500-1600 cm^{-1} are directly associated with the asymmetric stretching vibrations of the carboxyl groups found in the H_2BDC ligand that is incorporated into the MIL-101(Fe) framework. In contrast, the vibrational band located within the range of 1300-1400 cm^{-1} is correlated with the symmetrical stretching of carboxyl moieties present within the identical ligand and framework assemblage. Furthermore, the absorption band observed around 1600 cm^{-1} can be ascribed to the vibrational dynamics linked to the C = C bonds inherent in GO, a multifaceted substance extensively investigated for its distinctive characteristics and prospective utilizations. Lastly, the peak detected at approximately 3400 cm^{-1} is directly linked to the O-H stretching vibrations originating from water molecules that are adsorbed onto the surface of GO, indicating the presence of surface functional groups and interactions with the surrounding environment. This comprehensive analysis of various vibrational bands provides valuable information for characterizing and understanding the molecular structure and bonding interactions in these diverse materials.

Raman spectroscopy played a crucial role in validating the structural phase of the catalysts under investigation. The analysis of the resulting peak derived from MIL-101 (Fe)-NH_2 revealed significant vibrational features, with the prominent vibrational band observed at 660 cm^{-1} being attributed to NH_2 vibrations. Furthermore, additional vibrational bands at 1618, 1461, 1149, and 873 cm^{-1} were detected, providing strong evidence for the presence of aromatic and dicarboxylate groups within the H2BDC framework. Upon further examination of MIL-101 (Fe)-NH_2-GO-Fe_3O_4 photocatalysts with varying compositions (5%, 10%, and 20%), it was observed that the vibrational bands associated with MIL-101 (Fe)-NH_2 remained consistent, indicating the presence of NH_2 vibrations, aromatic groups, and dicarboxylate moieties from H_2BDC. Additionally, a distinct vibrational band at 1350 cm^{-1} corresponding to GO and Fe_3O_4 was identified, as illustrated in Figure 3 of the study.

A SEM was utilized to analyze the surface structure of the photocatalyst particles, revealing that the iron oxide particles exhibit a spherical morphology. Furthermore, these particles are found to be within the nanoscale range and have been successfully integrated onto GO, MIL-101(Fe), and MIL-101-(Fe) NH_2. Moreover, the research findings have established that the average dimensions of the GO and Fe_2O_3 sheets are approximately 30 and 25 nm, respectively, as illustrated in Figure 4. This detailed examination sheds light on the precise characteristics of the photocatalyst particles and their interactions with different materials, contributing significantly to the understanding of their behavior in various applications.

The Tauc curve, a commonly utilized approach for determining band gap, utilizes the reflectance spectrum in order to calculate this parameter. Tauc, Davies, and Matt proposed the relationship $(\alpha h\nu)1/n=A(h\nu-E_g)$ to clarify this phenomenon, where h symbolizes Planck's constant, ν indicates the vibrational frequency, α represents the absorption coefficient, E_g

denotes the band gap, and A is the proportionality constant. In the particular scope of this investigation, where direct transmission was deemed a suitable mechanism, the value of n for the samples under scrutiny was established as 1/2. Subsequent to the collection of reflectance spectrum data, it is converted into the Kobelka-Munk function. The F $(R\infty)$ on the vertical axis of this function is directly linked to the absorption coefficient. Following this, the initial α in the Touch equation is substituted with F $(R\infty)$ to derive the revised expression: $(F(R\infty)h\nu)^2 = A(h\nu - E_g)$. This transformation facilitates a more detailed analysis of the band gap and absorption characteristics within the material.

The Kubelka-Munk equation is as follows:

$$F(R\infty)=(1-R^2)/2R \qquad (2)$$

It is stated that R represents the reflectance spectrum in percentage. Then $(F(R\infty)h\nu)^2$ will be drawn in terms of hν and the value of $(h\nu-(h\nu F(R\infty))^2)$ which is the tangent line at the bend point of the curve will be drawn and using the tangent line Drawn from the previous step, the energy value of the band gap is obtained from the point of intersection of the tangent line to the curve and the horizontal axis. The DRS spectrum is obtained by shining light on the surface of a solid material and measuring the amount of diffuse reflection or absorption of the sample in terms of wavelength and comparing it with a standard sample. Diffuse reflectance measurement is particularly suitable for evaluating the optical properties of powder materials. In this particular investigation, the determination of the band gap energy was carried out by analyzing the reflective spectrum that penetrates based on the Touch equation. The outcomes of these calculations have been meticulously presented in both Table 2 and Figure 5 for comprehensive examination and reference. A relevant and noteworthy study conducted by Lin and colleagues in the year 2020 delved into the band gap characteristics of MIL-101 (Fe), establishing it at a value of 2.41 eV initially [42]. Interestingly, as the concentration of GO increased to 10 wt%, there was noted a reduction in the band gap, down to 2.17 eV. Upon careful analysis of the findings derived from the present research endeavor, it is discerned that the MIL-NH_2-GO-Fe-10% catalyst exhibited the narrowest band gap, quantified at 1.68 eV. Conversely, the MIL-GO-Fe-20% photocatalyst was observed to possess the widest band gap, also measured at 1.76 eV. These comparative results shed light on the intriguing variations in band gap energies across different catalyst compositions, offering valuable insights for further exploration in this domain.

To further rationalize the effect of the amine functionalization of the undertaken material, Figure 6 is provided. It displays the UV-Vis absorption behaviors for the following samples: a) MIL101 (Fe)-GO-Fe_3O_4 10% and b) MIL101 (Fe)-NH_2-GO-Fe_3O_4 10%. Based upon the presented results, it is a foregone conclusion that, the MIL101 (Fe)-NH_2-GO-Fe_3O_4 10% species has a higher absorption in the range of 300-450 nm compared to its non-functionalized counterpart. This means that, the former material indeed may become highly active under the UVA light irradiation which make it more desirable to use.

Based on the BET/BJH results, these isotherms are placed in the type (IV) isotherm group for mesoporous materials with hysteresis loops in the range of $0.6 < p/p_o < 1$ according to the IUPAC contract. The nitrogen adsorption-desorption technique is a crucial method utilized for analyzing the physical characteristics of particulate materials. This methodology is commonly employed to determine the surface area, volume, and pore sizes of nanostructured materials. The International Union of Pure and Applied Chemistry (IUPAC) has established specific criteria for categorizing pore sizes and adsorption isotherms, delineating six distinct classifications. The Type I isotherm is characteristic of microspores, whereas Types IV and V are associated with mesoporous materials. In contrast, Types II, III, and VI denote various other nanoporous structures. The current study performed nitrogen adsorption measurements on degassed samples at a temperature of 77 K. The results from the BET and BJH analyses are presented in Table 3. The findings indicate that the synthetic catalysts exhibit type IV isotherms. Furthermore, the study indicates that the integration of GO and Fe_3O_4 into MIL-101(Fe) and MIL-101(Fe)-NH_2 leads to a reduction in surface area, pore volume, and average pore diameter (see Figure 7 and Table 3).

TGA was employed to assess the thermal characteristics of the synthesized specimens within a temperature interval of 25-800 °C at a rate of 10 min^{-1}. The TGA graph corresponding to the produced samples is depicted in Figure 8. In short, the TGA analysis provides information upon thermal stability, composition, decomposition stages, and residues, all of which are influenced by the material's chemical structure (bond strength, additives), physical structure (crystalline vs. amorphous), composition (fillers, impurities), and undergoing test conditions. This ultimately helps to understand how do materials behave under heat, which is indeed crucial for applications that require thermal resistance. According to the findings, the observed 20% reduction in weight of GO within the temperature spectrum of 150-20 °C is ascribed to the desorption of both surface and interlayer moisture. The thermal ranges of 200-300 °C are indicative of the degradation of epoxy functionalities within GO. In addition, a 34% weight loss is observed in the temperature range of 50-400 °C for the Go-Fe_3O_4 catalyst. In the scenario involving MIL-101(Fe)-NH2-Go-Fe3O4 catalysts with loadings of 5%, 10%, and 20%, the recorded weight reductions are 29.15%, 55.8%, and 60.98%, respectively. This increase in mass loss is clearly related to the added weight of Fe_3O_4.

In the realm of semiconductor physics, the Matt-Schottky curve serves as a crucial tool for distinguishing between positive and negative type semiconductors based on the direction of the slope [14]. Specifically, a negative slope within this curve signifies a positive type semiconductor, while a positive slope indicates a negative type semiconductor, reflecting the underlying electrical characteristics of the material under study. Furthermore, by analyzing the potential of the flat strip in relation to the intersection of the linear portion of the Matt-Schottky curve, one can discern the nature of the semiconductor material, with a negative slope once again pointing towards a positive type semiconductor, thereby providing valuable insights into its behavior and properties. In Figures 9 a) and, b), it can be observed that the slopes associated with the Schottky matte data pertaining to GO and MIL-101-NH_2 exhibit distinct characteristics: a positive slope for GO and a negative slope for MIL-101-NH_2. These opposing slopes serve as indicators of the respective types of conductivity, with the positive slope indicative of p-type conductivity and the negative slope suggestive of n-type conductivity. The outcomes of the study reveal that the MIL-101-(Fe) NH_2-GO-Fe_3O_4 10% photocatalyst displays both negative and positive slopes, suggesting the presence of a p-n heterogeneous junction, as illustrated in Figure 9. This intricate heterojunction structure is a key factor in determining the efficiency and effectiveness of the photocatalytic process in transforming CO_2 into methanol (Figure 9 c).

The figure illustrating the oscillating magnetometer graph of the nanocomposite MIL-101 (Fe)-NH_2-GO-Fe_3O_4 10% is presented in Figure 10. Upon analysis of the oscillating magnetometer curve pertaining to the nanocomposite MIL-101 (Fe)-NH_2-GO-Fe_3O_4 10%, it can be deduced that the curve exhibits characteristics such as a hysteresis loop, hysteresis, and anti-hysteresis field. These features are indicative of the fact that these materials necessitate a magnetic field for magnetization and demonstrate a tendency to retain their magnetic properties, thereby classifying them as materials possessing magnetic characteristics. The particles within this nanocomposite exhibit properties of ferromagnetism, highlighting their magnetic nature. It is noteworthy that this compound displays a saturation magnetization value of 8.59 emu/g, underscoring its magnetic behavior and further emphasizing its suitability for various applications involving magnetic properties. In the pursuit of examining the influence of catalyst type on the process, a series of experiments were meticulously carried out, leading to the revelation that among the tested catalysts, the photocatalyst MIL-101 (Fe)-NH_2-GO-Fe_3O_4 10% emerged as the most efficient performer in the realm of methanol production, as visually depicted in Figure 11. Accordingly, the BET/BJH results provided earlier revealed that, through modifying the photocatalyst surface with the NH_2 group, the surface area was enhanced while the UV-Vis analysis displayed that, the adsorption band gap was reduced. Both these findings confirmed that, an increase in the photocatalytic efficiency should be expected.

3.2 Design of Experiment

In the present investigation, the impacts of various variables such as time in minutes, mass of catalyst in grams, Fe_3O_4 weight percentage in wt%, and pH were examined across three different levels. Following the completion of the experimental procedures, it was observed that the maximum rate of methanol production reached 2896 mg/L. The visual representation portrayed in Figure 12 a) offers a graphical depiction of the assumption related to the normal distribution of the data, suggesting a closeness to a Gaussian distribution. Moreover, the results indicate a conformity of the residuals to a The Gaussian distribution pattern reveals a significant association between the outcomes derived from the experimental approach and the values anticipated through statistical methodologies. This alignment between the empirical data and statistically forecasted values signifies a high degree of agreement and dependability in the analysis that was carried out. These findings emphasize the robustness of the relationship between the variables studied and the outcomes generated, enhancing the credibility and validity of the research findings. The thorough evaluation of the experimental variables at different levels has contributed to a deeper understanding of the factors influencing the production rate of methanol, shedding light on the intricacies of the catalytic process involved in the study. Overall, the outcomes of this study underscore the importance of integrating empirical observations with statistical analyses to achieve a comprehensive and insightful understanding of the phenomena under investigation. In Table 4, the selected model, which is of the second degree of significance, proves to be suitable for the data. T and P are interconnected, displaying similarities in statistical results. Larger T-Value absolute values correspond to smaller P-values, decreasing the likelihood of accepting the null hypothesis. Empirical research is conventionally performed at a confidence threshold of 95%, where a P-value lower than 0.05 results in the dismissal of the null hypothesis. Regression seeks to minimize the disparity between actual and estimated values, with the objective of decreasing the total sum of squared residuals. R-Squared measures data proximity to the regression line, with Adj R-Squared differing by considering only actual independent variable effects on the dependent variable. The results of the ANOVA analysis indicated R-Squared and Adjusted R-Squared values of 0.9446 and 0.8529, respectively, which demonstrate the accuracy of the model. The significance of the factors pH, weight percentage of Fe_3O_4, mass of the catalyst, and duration was assessed and ranked accordingly (Figure 12 b).

3.3 Effect factors in photocatalytic conversion

The effect of varying the dosage of the photocatalyst on the photocatalytic conversion of CO_2 to methanol was examined by modifying the quantity of photocatalyst used, ranging from 0.1 to 1 g, under UVA irradiation. Upon 2 hours of UVA light exposure, Figure 13 illustrates the progression of methanol production through photocatalysis. The production of methanol exhibited a steady rise as the amount of catalyst increased from 0.1 to 0.5 g. An elevation in the concentration of the photocatalyst in the solution is associated with a rise in the overall quantity of active sites present on the surface of the photocatalyst, as demonstrated in Figure 14. As a result, the effectiveness of the photocatalyst is improved owing to the increased availability of active sites for the conversion process. Figure 13 shows the amount of CO_2 oxidative removal in a period of 2 h. The results of this investigation show that at the beginning of the reaction, it started with a relatively fast rate; until it reaches its highest level after 2 h from the start of the reaction. The obtained results showed that the conversion rate is high in the initial times, which can be caused by the high catalytic level and the volume of holes at the beginning of the work. With the passage of time and the transformation of the pollutant on the catalyst, the holes of the catalyst are gradually filled and the production efficiency decreases.

The reaction of reducing CO_2 to fuel at different initial pH is shown in Figure 13. Changing the pH has an obvious effect on the efficiency of those compounds. Higher yields were obtained when tests were performed in acidic solutions than in alkaline solutions (Figure 13).

Low pH enhances proton concentration, potentially lowering the theoretical reduction potential of CO_2 by facilitating electron transfer via protonation, while carbonate and bicarbonate species present greater reduction challenges and may act as hole scavengers, rendering their effect negligible in acidic solutions, thereby favoring reductions at pH 5. In order to examine the impact of varying weight percentages of Fe_3O_4, several different ratios such as 5%, 10%, and 20% were introduced into the experimental reaction setup. The findings revealed that elevating the weight percentage of iron oxide from 5% to 10% resulted in a reduction in the band gap, alongside an enhancement in electron and hole transfer processes within the photocatalytic activity. Conversely, a subsequent increase in the weight percentage of iron oxide from 10% to 20% led to an expansion in the band gap, coupled with a decline in both electron and hole transfer efficiencies (Figure 13). This experimental data highlights the critical role played by the weight percentage of Fe_3O_4 in influencing the photochemical properties of the reaction system.

Under optimal conditions, the synthesis of methanol was enhanced by the application of 0.46 g of MIL-101(Fe)-NH_2-GO-Fe_3O_4 (7.82%) as a photocatalyst over a time span of 107 minutes at a pH of 5, yielding a methanol concentration of 2978.25 mg/L (Figure 14). Under ideal experimental conditions, the photocatalytic conversion assessment was executed, and the findings revealed the generation of methanol quantified at 2965.06 mg/L, which is significantly aligned with the optimal parameters established by the computational software. Also, Under ideal circumstances, the conversion efficiency and selectivity were assessed, revealing that the conversion efficiency of CO_2 to methanol attained a remarkable 91%, with a selectivity of 83%.

After performing the photocatalytic process in optimal conditions, the resulting sample was detected in the GC-MS machine. Based on the results, the sample contains methanol, formamide and formaldehyde (Figure 15).

3.4 Mechanism of conversion

It is essential to comprehensively assess the photocatalytic reduction mechanism of CO_2 to methanol within aqueous systems, and to meticulously examine the potential reactions that could transpire following the absorption of photons possessing specific energy levels. The magnitude of the band gap inherent to the employed photocatalyst is pivotal in the aforementioned process. In this investigation, the absorption of light photons, possessing energy levels that are equivalent to or exceed the band gap energy of the 10% MIL-101(Fe)-NH_2-GO-Fe_3O_4 photocatalyst, triggers the excitation of electrons (e^-) and the formation of hole pairs (h^+), which are subsequently elevated to the unoccupied conduction band (CB) and the available valence band (VB), correspondingly, thereby enhancing the generation of energetic charge carriers that are integral to ensuing chemical transformations. The highly energetic charge carriers, upon their generation, serve as catalysts for a sequence of intricate redox reactions that ultimately culminate in the synthesis of the target final products. In this framework, equations (3) and (4) delineate the specific activation reactions pertinent to the 10% MIL-101(Fe)-NH_2-GO-Fe_3O_4 semiconductor, thereby enhancing the comprehension of the fundamental mechanisms operating within this photocatalyst.

$$\text{MIL-101(Fe)-NH}_2\text{-GO-Fe}_3\text{O}_4\ 10\% + h\upsilon\ (\geq E_g) \rightarrow h + e^- \quad (3)$$

$$h^+e^- \longrightarrow h^+ VB + e^- CB \quad (4)$$

Charge carriers produced via the photocatalytic mechanism may take several distinct pathways, each characterized by specific mechanisms and interactions that ultimately increase the overall efficiency of photocatalytic processes. After a comprehensive review of previous experimental research, it has been found that the products resulting from CO_2 conversion often have significant similarities with traditional reactions, which are, however, limited to CO, HCOOH, HCHO, CH_3OH, CH_4 and C2H5OH, as a result of the potential of these compounds. They emphasize to act as efficient reducing agents in a variety of chemical reactions. The process of photocatalytic oxidation of water occurs as a result of the direct exposure of light to the surface of the magnetic semiconductor MIL-101 (Fe)-NH_2-GO-Fe_3O_4 at a concentration of 10%. This mechanism leads to the generation of highly reactive hydroxyl radicals, while simultaneously promoting the production of hydrogen ions (H^+) by harnessing electrons obtained from the conduction of hydrogen bonds. Consequently, this mechanism enhances the overall photochemical efficiency of the system.

4. Conclusion

The study focused on the photocatalytic conversion of CO_2 into fuel utilizing synthetic catalysts. The analysis explored the effects of surface modification of MIL-101 (Fe) with amine groups on methanol synthesis. The study focused on the photocatalytic conversion of CO2 into fuel utilizing synthetic catalysts. A thorough examination of the data revealed that the MIL-101(Fe)-NH_2-GO-Fe_3O_4 10% photocatalyst establishes a p-n heterojunction. In optimal circumstances, methanol synthesis was accomplished utilizing 0.46 grams of MIL-101(Fe)-NH_2-GO-Fe_3O_4 (7.82%) as a photocatalyst over a duration of 107 minutes at a pH of 5, yielding a concentration of 2978.25 mg/L. Subsequent to the photocatalytic process conducted under optimal conditions, the product was identified through GC-MS. The examination indicated the detection of methanol, formamide, and formaldehyde within the specimen. In summary, it can be deduced from the findings that the transformation of CO_2 into methanol utilizing the MIL-101-(Fe) GO-Fe_3O_4 7.82% catalyst constitutes a mild, efficient, and economically viable methodology.

Conflict of Interests

On behalf of all contributors, the corresponding authors affirm that there are no conflicts of interest to disclose.

References

1. Marcos, F. C. F., Costa, M. J. F., Catuzo, G. L., et al., "Supported Cu catalysts on UiO-66 toward enhanced methanol selectivity by CO2 hydrogenation: effect of Cu loading". *Journal of Catalysis*, **427**, pp. 115104 (2023). https://doi.org/10.1016/j.jcat.2023.115104.
2. Merino-Garcia, I., García, G., Hernández, I., et al., "An optofluidic planar microreactor with photoactive Cu2O/Mo2C/TiO2 heterostructures for enhanced visible light-driven CO2 conversion to methanol". *Journal of CO2 Utilization*, **67**, pp. 102340 (2023). https://doi.org/10.1016/j.jcou.2022.102340.
3. Yap, P. L., Nguyen, H. H., Ma, J., et al., "Exploring kinetic and thermodynamic insights of graphene related two dimensional materials for carbon dioxide adsorption". *Separation and Purification Technology*, **348**, pp. 127633 (2024). https://doi.org/10.1016/j.seppur.2024.127633.
4. Tahir, M., Ajiwokewu, B., Bankole, A. A., et al., "MOF based composites with engineering aspects and morphological developments for photocatalytic CO2 reduction and hydrogen production: A comprehensive review". *Journal of Environmental Chemical Engineering*, **11**(2), pp. 109408 (2023). https://doi.org/10.1016/j.jece.2023.109408.
5. Shi, H., Tian, C., Liu, X., et al., "Ni-phyllosilicate nanotubes coated by CeO2 for ultra-efficiency of 36.9% and near-limit CO2 conversion in solar-driven conversion

of CO2-to-fuel". *Chemical Engineering Journal*, **454**, pp. 140063 (2023). https://doi.org/10.1016/j.cej.2022.140063.

6. Gulati, S., Vijayan, S., Kumar, S., et al., "Recent advances in the application of metal-organic frameworks (MOFs)-based nanocatalysts for direct conversion of carbon dioxide (CO2) to value-added chemicals". *Coordination Chemistry Reviews*, **474**, pp. 214853 (2023). https://doi.org/10.1016/j.ccr.2022.214853.
7. Li, J., Luo, H., Li, B., et al., "Application of MOF-derived materials as electrocatalysts for CO 2 conversion". *Materials Chemistry Frontiers*, **7**(23), pp. 6107-6129 (2023). https://doi.org/10.1039/D3QM00835E.
8. Sun, X., Ji, M., Zhang, Y., et al., "In-situ embedded ultrafine Bi12O17Br2 nanotubes in MOF-derived hierarchical porous carbon for enhanced photocatalytic CO2 conversion to CO". *Journal of Materials Science & Technology*, **171**, pp. 47-53 (2024). https://doi.org/10.1016/j.jmst.2023.05.075,
9. Fard, N. E., Ali, N. S., Saady, N. M. C., et al., "A Review on Development and Modification Strategies of MOFs Z-scheme Heterojunction for Photocatalytic Wastewater Treatment, Water Splitting, and DFT Calculations". *Heliyon*, 2024. ht.tps://doi.org/10.1016/j.heliyon.2024.e32861
10. Gharagozlou, M., Fard, N. E., Ghahari, M., et al., "Bimetal Cu/Ni-BTC@ SiO2 metal-organic framework as high performance photocatalyst for degradation of azo dyes under visible light irradiation". *Environmental Research*, pp. 119229 (2024). https://doi.org/10.1016/j.envres.2024.119229.
11. Liu, J., Zheng, Y., Zhu, Q., et al., "MnO x–CeO 2 Derived from Mn–Ce-MOFs with Highly Efficient Removal of Formaldehyde". *Catalysis Surveys from Asia*, **24**, pp. 207-218 (2020). https://doi.org/10.1007/s10563-020-09301-9.
12. Erfani Gahrouei, A., Kazemeini, M., Jahangirifard, S., et al., "A performance-based comparison for the synthesis of Plavix (Clopidogrel) in a microreactor vs. batch reactor: From CuBr2 homogeneous catalysis to heterogeneous catalysis using a Cu-based MOF (VNU-18)". *Scientia Iranica*, 2024. https://doi.org/10.24200/sci.2024.63474.8414
13. Liu, L., Zhang, J., Cheng, X., et al., "Amorphous NH2-MIL-68 as an efficient electro-and photo-catalyst for CO2 conversion reactions". *Nano Research*, **16**(1), pp. 181-188 (2023). https://doi.org/10.1007/s12274-022-4664-0.
14. Fard, N.E., H. Pasdar, and M.T. Yaraki, "CdSe nanoflower as a new near infrared-activated photocatalyst for remediation of pharmaceutical wastewaters". *Materials Today Sustainability*, pp. 100961 (2024). https://doi.org/10.1016/j.mtsust.2024.100961.
15. Ikreedeegh, R. R., Hossen, M. A., Sherryna, A., et al., "Recent advances on synthesis and photocatalytic applications of MOF-derived carbon materials: A review". *Coordination Chemistry Reviews*, **510**, pp. 215834 (2024). https://doi.org/10.1016/j.ccr.2024.215834.
16. Esfahani, H.J., S. Shahhosseini, and Ghaemi, A. "Improved structure of Zr-BTC metal organic framework using NH2 to enhance CO2 adsorption performance". *Scientific Reports*, **13**(1), pp. 17700 (2023). https://doi.org/10.1038/s41598-023-44076-9.

17. Ren, X., Wang, C. C., Li, Y., et al., "Defective SO3H-MIL-101 (Cr) for capturing different cationic metal ions: Performances and mechanisms". *Journal of Hazardous Materials*, 2023. **445**, pp. 130552 (2023). https://doi.org/10.1016/j.jhazmat.2022.130552.

18. Wang, C. Y., Wang, C. C., Chu, H. Y., et al., "In situ growth of MIL-101 (Fe) on waste PET plastic slices for effective arsenic removal". *Separation and Purification Technology*, **331**, pp. 125589 (2024). https://doi.org/10.1016/j.seppur.2023.125589.

19. Lighvan, Z. M., Hosseini, S. R., Norouzbahari, S., et al., "Synthesis, characterization, and selective gas adsorption performance of hybrid NH2-MIL-101 (Fe)/ZIF-8 metal organic framework (MOF)". *Fuel*, **351**, pp. 128991 (2023). https://doi.org/10.1016/j.fuel.2023.128991.

20. Luo, Y. and R. Su, "Preparation of NH2-MIL-101 (Fe) metal organic framework and its performance in adsorbing and removing tetracycline". *International Journal of Molecular Sciences*, **25**(18), pp. 9855 (2024). https://doi.org/10.3390/ijms25189855.

21. Vinothkumar, K. and R.G. Balakrishna, "One-pot synthesis of NH2-MIL-101 (Fe) and α–Fe2O3 composite as efficient heterojunction for multifunctional photocatalytic membranes: Towards zero waste generation". *Applied Catalysis B: Environmental*, **340**, pp. 123199 (2024). https://doi.org/10.1016/j.apcatb.2023.123199

22. Song, X., Zhu, T., Yu, S., et al., "A novel nitrogenous core-shell MIL-101 (Fe)-based nanocomposite for enhanced adsorption and photo-degradation of organic pollutant under visible light". *Journal of Alloys and Compounds*, **938**, pp. 168479 (2023). https://doi.org/10.1016/j.jallcom.2022.168479.

23. Wang, H., Tu, H., Chen, F., et al., "Construction of highly dispersed NH2-MIL-101 (Fe)/g-C3N4 heterostructure with excellent photocatalytic redox capability". *Journal of Environmental Chemical Engineering*, **11**(3), pp. 109663 (2023). https://doi.org/10.1016/j.jece.2023.109663.

24. Zhu, H., Xue, S., Zhao, F., et al., "MIL-101 (Fe)@ Nb2C MXene for efficient electrocatalytic ammonia production: an experimental and theoretical study". *New Journal of Chemistry*, **47**(32), pp. 15302-15308 (2023). https://doi.org/10.1039/D3NJ02436A.

25. Ji, W., Li, W., Wang, Y., et al., "Zr-doped MIL-101 (Fe)/Graphene oxide nanocomposites: An efficient and water-stable MOF-based adsorbent for As (V) adsorption in aqueous solution". *Separation and Purification Technology*, **339**, pp. 126681 (2024). https://doi.org/10.1016/j.seppur.2024.126681.

26. Chen, J., Li, Z., Li, X., et al., "A reverse-signal response fluorescence sensor based on NH2-MIL-101 (Fe) and silicon-doped carbon quantum dots for selective determination of copper ions". *Journal of Photochemistry and Photobiology A: Chemistry*, **452**, pp. 115579 (2024). https://doi.org/10.1016/j.jphotochem.2024.115579.

27. Larasati, L., Dendy, D., Lestari, W. W., et al., "Rapid and Facile Electrochemical Synthesis of MIL-101 (Fe)-NH2 and Its Curcumin Loading and Release Studies". *Journal of Inorganic and Organometallic Polymers and Materials*, pp. 1-11 (2024). https://doi.org/10.1007/s10904-024-03049-9.

28. Mahdipoor, H. R., Halladj, R., Babakhani, E. G., et al., "Adsorption of CO2, N2 and CH4 on a Fe-based metal organic framework, MIL-101 (Fe)-NH2". *Colloids and*

Surfaces A: Physicochemical and Engineering Aspects, **619**, pp. 126554 (2021). https://doi.org/10.1016/j.colsurfa.2021.126554

29. Huang, P., Yao, L., Chang, Q., et al., "Room-temperature preparation of highly efficient NH2-MIL-101 (Fe) catalyst: The important role of–NH2 in accelerating Fe (III)/Fe (II) cycling". *Chemosphere*, **291**, pp. 133026 (2022). https://doi.org/10.1016/j.chemosphere.2021.133026.

30. Saeed, M., S. Alduwaib, and D. Al-den, "Investigation of structural, photo-luminescence and self-cleaning properties of thin layers of GO-ZnO and GO, GO-Ag and composite bilayer of GO-ZnO/GO-Ag prepared by spray pyrolysis method". *Scientia Iranica*, **31**(12), pp. 958-966 (2024). http://doi.org/10.24200/sci.2023.61099.7140.

31. Meng, Z., Yu, B., Chen, Y., et al., "The high content of NH2-MIL-101 (Fe) in NH2-MIL-101 (Fe)/Fe3O4/GO enables selective adsorption removal of five parabens". *Chemical Engineering Science*, **284**, pp. 119527. (2024). https://doi.org/10.1016/j.ces.2023.119527.

32. Vandani, S. A. K., Kalaee, M., Saravani, M. G., et al., "Preparation of magnetic Fe3O4/MoO3/MCM-22 photocatalyst and its study on metronidazole adsorption, degradation, and process optimization". *Russian Journal of Physical Chemistry A*, **97**(4), pp. 618-632 (2023). https://doi.org/10.1134/S003602442304026X.

33. Elmi Fard, N. and R. Fazaeli, "Fabrication of superhydrophobic CoFe2O4/polyaniline/covalent organic frameworks/cotton fabric membrane and evaluation of its efficiency in separation of olive oil from water". *Journal of the Chinese Chemical Society*, **69**(12), pp. 2014-2026 (2022). https://doi.org/10.1002/jccs.202200368.

34. Xing, Y., Si, H., Sun, D., et al., "Magnetic Fe3O4@ NH2-MIL-101 (Fe) nanocomposites with peroxidase-like activity for colorimetric detection of glucose". *Microchemical Journal*, **156**, pp. 104929. (2020). https://doi.org/10.1016/j.microc.2020.104929.

35. He, X., Zhou, Y., Yang, W., et al., "Microwave assisted magnetic solid phase extraction using a novel amino-functionalized magnetic framework composite of type Fe3O4-NH2@ MIL-101 (Cr) for the determination of organochlorine pesticides in soil samples". *Talanta*, **196**, pp. 572-578. (2019). https://doi.org/10.1016/j.talanta.2018.12.019.

36. Shahi, M.S.M., L. Vafajoo, and M. Kazemeini, "Physiochemical Evaluation of a Ternary Magnetic MIL-101 (Fe)–GO–Fe3O4 Utilized for Photocatalytic Conversion of CO2 into Methanol under Ultraviolet Light Irradiation". *Russian Journal of Physical Chemistry A*,. **97**(7), pp. 1601-1614 (2023). https://doi.org/10.1134/S0036024423070178.

37. Arash, A. and Vafajoo, L. "Photocatalytic CO2 reduction of amino-functionalized MIL-101 (Fe) coupled with reduced graphene oxide under UV–visible light illumination". Reaction Kinetics, *Mechanisms and Catalysis*, **137**(3), pp. 1789-1803 (2024). https://doi.org/10.1007/s11144-024-02588-z

38. Fard, N. E., Fazaeli, R., Yousefi, M., et al., "Oxidative desulfurization of dibenzothiophene using M/TiO2/MWW (M= Cu, Ag, and Au) composite". *Russian*

Journal of Physical Chemistry A, **95**(Suppl 1), pp. S23-S32 (2021). https://doi.org/10.1134/S0036024421140065.

39. Fekra, S.S., N.E. Fard, and R. Fazaeli, "Photocatalytic degradation of antibiotic norfloxacin aqueous solution by Ce/Bi2WO6: optimization and simulation of process by RSM". *Russian Journal of Applied Chemistry*, **94**(6), pp. 824-834 (2021). https://doi.org/10.1134/S1070427221060161.
40. Hassan, S. U., Shafique, S., Palvasha, B. A., et al., "Photocatalytic degradation of industrial dye using hybrid filler impregnated poly-sulfone membrane and optimizing the catalytic performance using Box-Behnken design". *Chemosphere*, **313**, pp. 137418 (2023). https://doi.org/10.1016/j.chemosphere.2022.137418.
41. Yousefi, M., Akbari, H., Adibzadeh, A., et al., "Adsorption of diazinon from aqueous solution using metal organic framework and functionalized graphene: Comparison of BBD, ANN models". *Chemosphere*, **351**, pp. 141222 (2024). https://doi.org/10.1016/j.chemosphere.2024.141222.
42. Lin, J., Hu, H., Gao, N., et al., "Fabrication of GO@ MIL-101 (Fe) for enhanced visible-light photocatalysis degradation of organophosphorus contaminant". *Journal of Water Process Engineering*, **33**, pp. 101010 (2019). https://doi.org/10.1016/j.jwpe.2019.101010.

List of Figure Captions

Figure 1. XRD pattern for photocatalysts

Figure 2. FTIR peaks for photocatalysts.

Figure 3. RAMAN peaks for photocatalysts.

Figure 4. SEM images of photocatalysts (a GO, (b GO-Fe_3O_4, (c MIL-101-GO-Fe_3O_4, (d MIL-101-(Fe) NH_2) and e) MIL-101 (Fe)-NH_2-GO-Fe_3O_4.

Figure 5. Band gap (a MIL-GO-Fe-5%, (b MIL-GO-Fe-10%, (c MIL-GO-Fe-20%, (d MIL-NH_2-GO-20%, (e MIL- NH_2-GO-Fe-10% and (f MIL-NH_2-GO-Fe-20%.

Figure 6. UV-Vis for a) MIL101 (Fe)-GO-Fe_3O_4 10% and b) MIL101 (Fe)-NH_2-GO-Fe_3O_4 10%.

Figure 7. BET-BJH results (a MIL-101 (Fe), (b GO, (c GO-Fe_3O_4, (d MIL-101 (Fe)-NH_2-GO-Fe_3O_4 5%, (e MIL-101 (Fe)-NH_2-GO-Fe_3O_4 10%) and (f MIL-101 (Fe)-NH_2-GO-Fe_3O_4 20%.

Figure 8. TGA results for photocatalysts.

Figure 9. Matt-Schottky for GO ،(b MIL-101-NH_2 and (c MIL-101-NH_2-GO-Fe_3O_4 10%.

Figure 10. VSM for MIL-101-NH_2-GO-Fe_3O_4 10%.

Figure 11. Effect of catalyst type on methanol production.

Figure 12. a) Normal probability plot of the studentized residual for photocatalytic degradation and b) The effect of influencing factors in the process.

Figure 13. Effect of a) mass of catalyst and time, b) pH and time, c) Fe_3O_4 weight percentage and time.

Figure 14. Optimal conditions for fuel production.

Figure 15. GC-MS results after photocatalytic reaction.

List of Table Captions

Table 1. Experiments designed with the RSM.

Table 2. DRS results of synthetic photocatalysts.

Table 3. BET-BJH results of photocatalysts.

Table 4. ANOVA for analysis of variance and adequacy of the quadratic model.

Figures

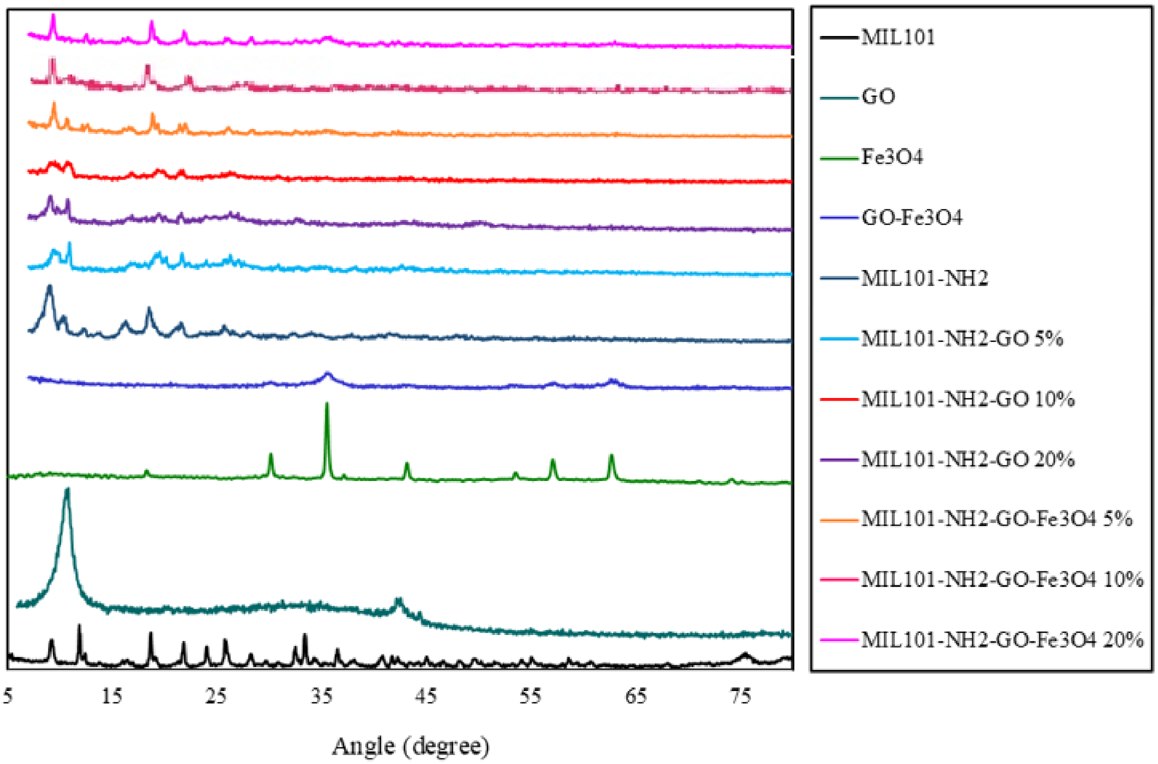

Figure 1.

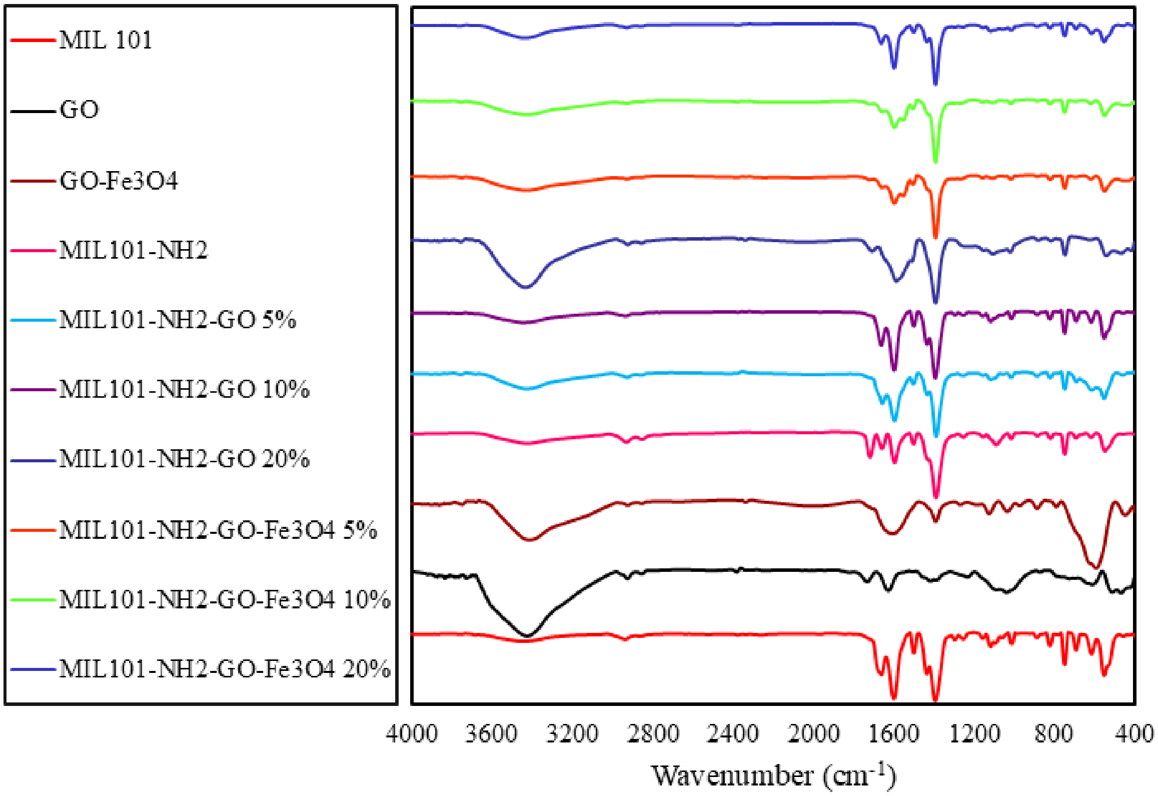
MIL 101
GO
GO-Fe3O4
MIL101-NH2
MIL101-NH2-GO 5%
MIL101-NH2-GO 10%
MIL101-NH2-GO 20%
MIL101-NH2-GO-Fe3O4 5%
MIL101-NH2-GO-Fe3O4 10%
MIL101-NH2-GO-Fe3O4 20%
4000
3600
3200
2800
2400
2000
1600
1200
800
400
Wavenumber (cm-1)

Figure 2.

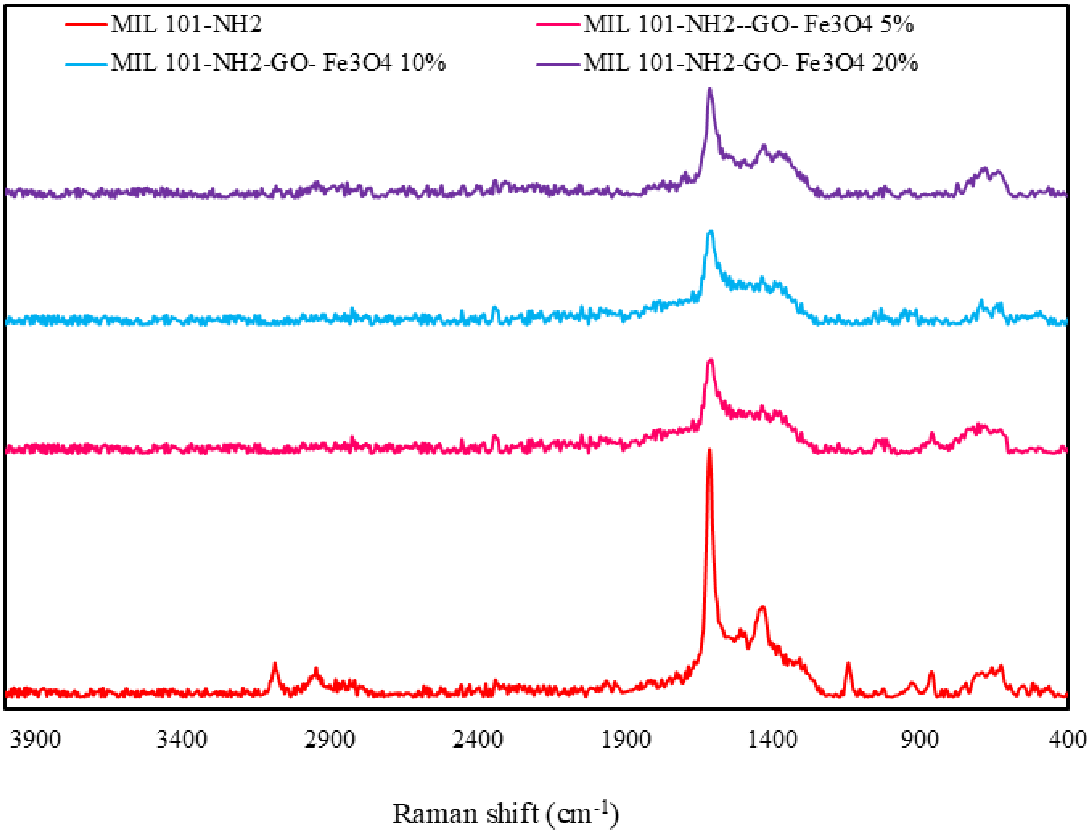

Figure 3.

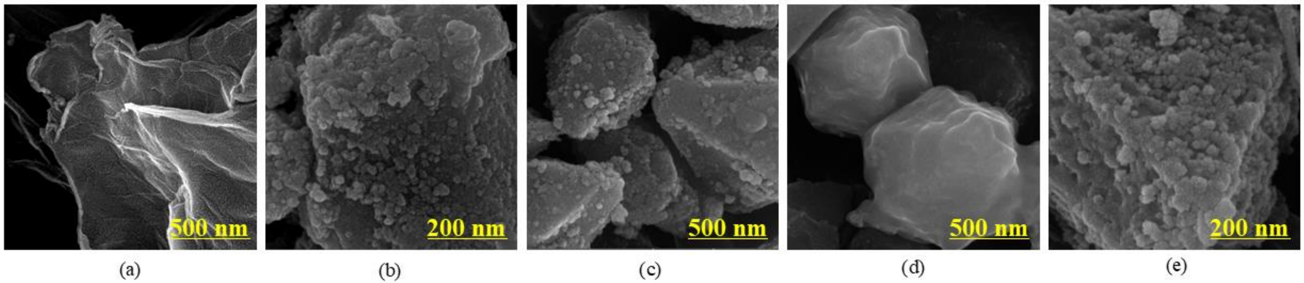

(a) (b) (c) (d) (e)

Figure 4.

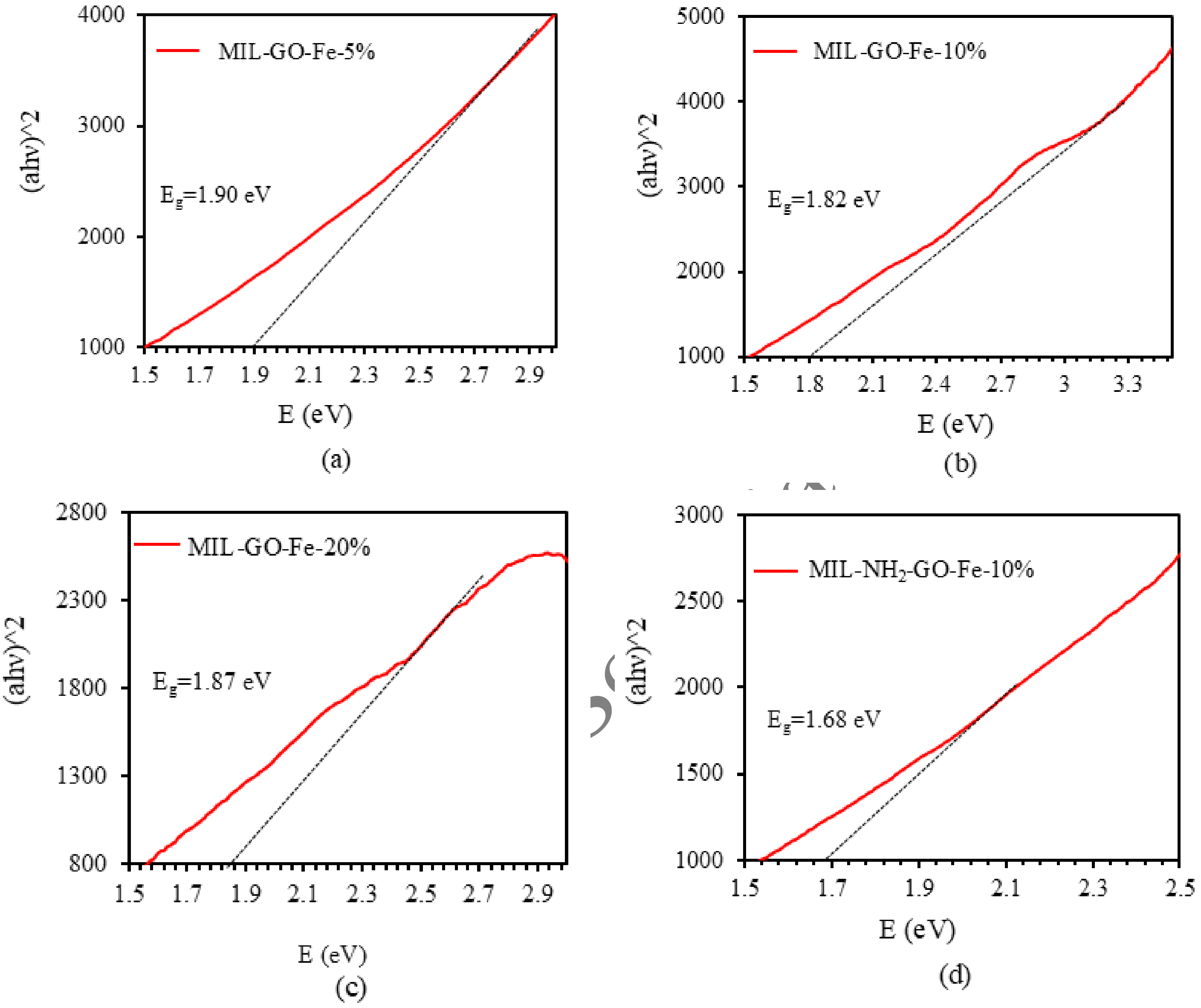
(a)
MIL-GO-Fe-5%
E_g=1.90 eV
(ahν)^2
4000
3000
2000
1000
1.5
1.7
1.9
2.1
2.3
2.5
2.7
2.9
E (eV)
(b)
MIL-GO-Fe-10%
E_g=1.82 eV
(ahν)^2
5000
4000
3000
2000
1000
1.5
1.8
2.1
2.4
2.7
3
3.3
E (eV)
(c)
MIL-GO-Fe-20%
E_g=1.87 eV
(ahν)^2
2800
2300
1800
1300
800
1.5
1.7
1.9
2.1
2.3
2.5
2.7
2.9
E (eV)
(d)
MIL-NH$_2$-GO-Fe-10%
E_g=1.68 eV
(ahν)^2
3000
2500
2000
1500
1000
1.5
1.7
1.9
2.1
2.3
2.5
E (eV)

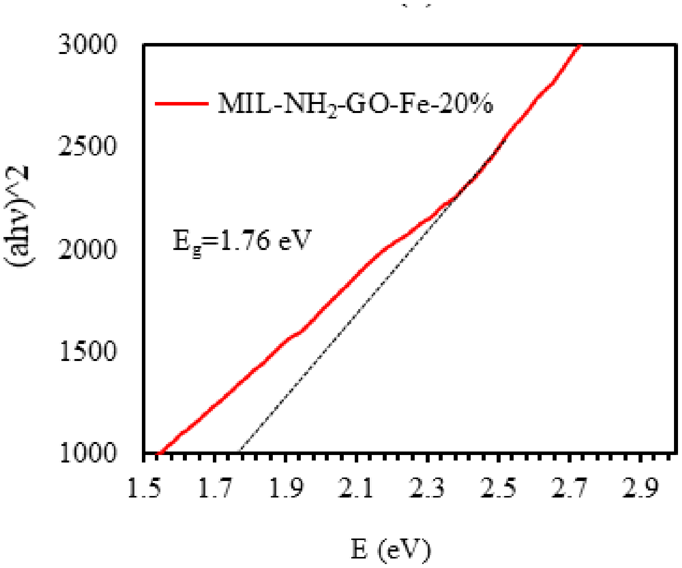
3000
2500
2000
1500
1000
(ahv)^2
MIL-NH$_2$-GO-Fe-20%
E$_g$=1.76 eV
1.5
1.7
1.9
2.1
2.3
2.5
2.7
2.9
E (eV)

(e)

Figure 5.

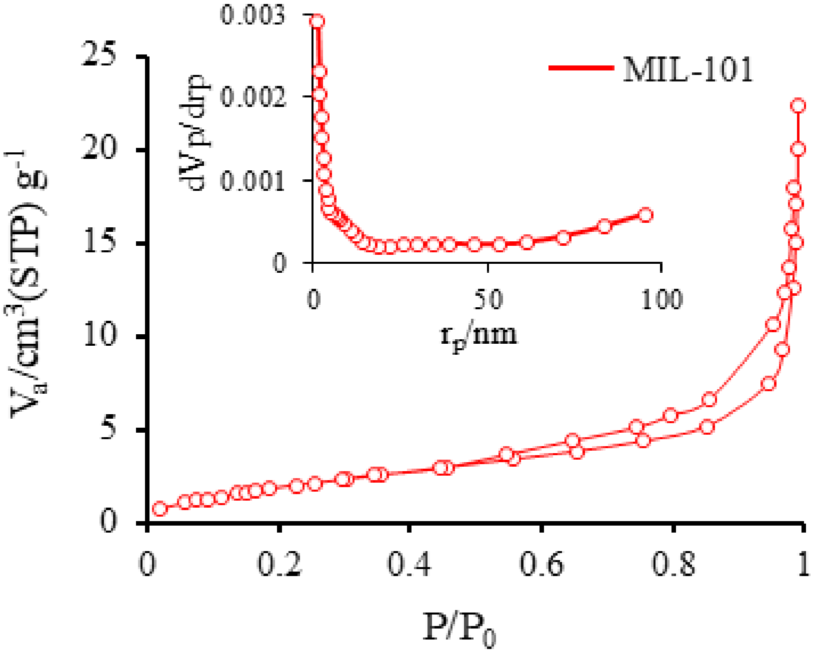
MIL-101
$V_a/cm^3(STP)\ g^{-1}$
0
5
10
15
20
25
0
0.2
0.4
0.6
0.8
1
P/P_0
dVp/drp
0
0.001
0.002
0.003
0
50
100
r_p/nm

(a)

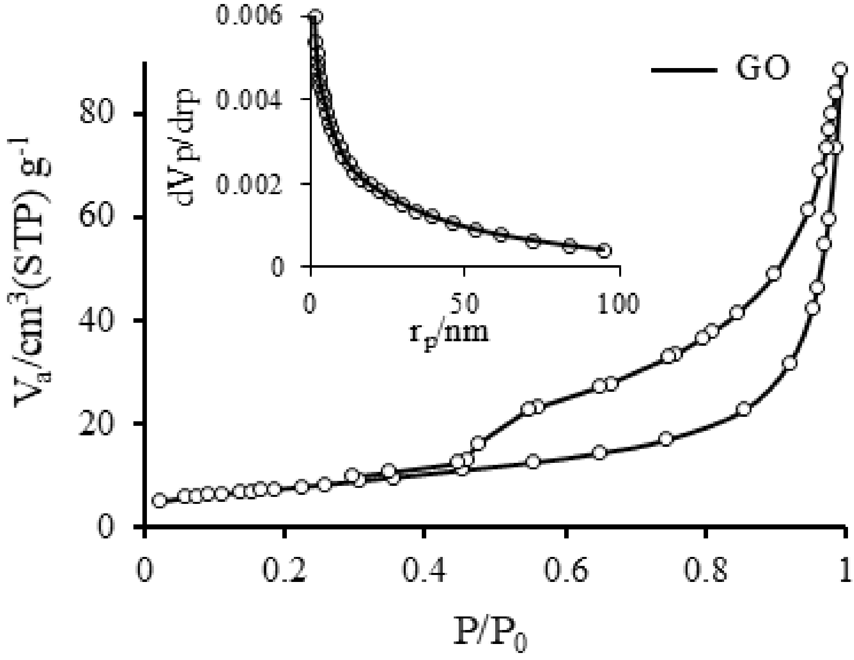
GO
$V_a/cm^3(STP)\ g^{-1}$
0
20
40
60
80
0
0.2
0.4
0.6
0.8
1
P/P_0
dVp/drp
0
0.002
0.004
0.006
0
50
100
r_p/nm

(b)

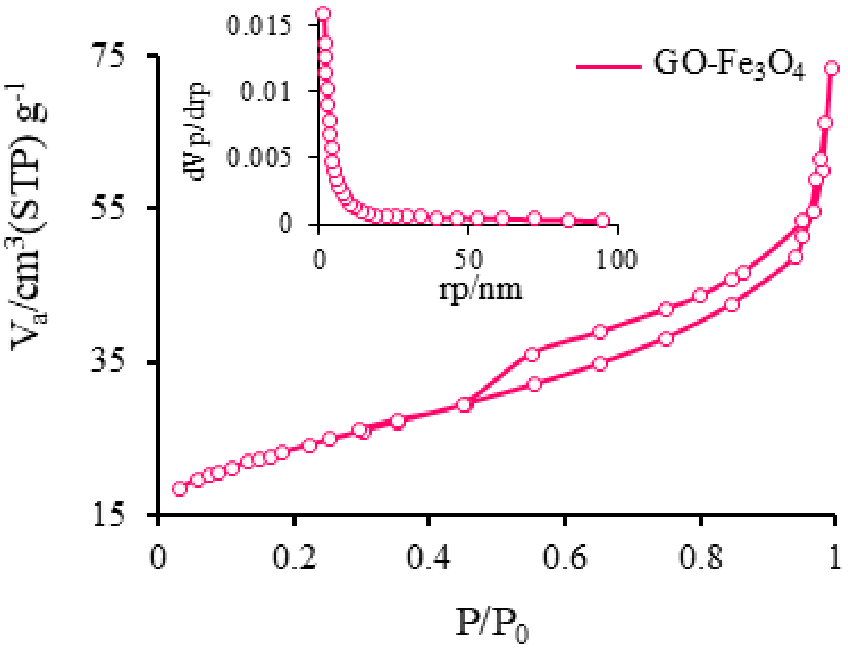
GO-Fe3O4
Va/cm3(STP) g-1
75
55
35
15
0
0.2
0.4
0.6
0.8
1
P/P0
dVp/drp
0.015
0.01
0.005
0
0
50
100
rp/nm

(c)

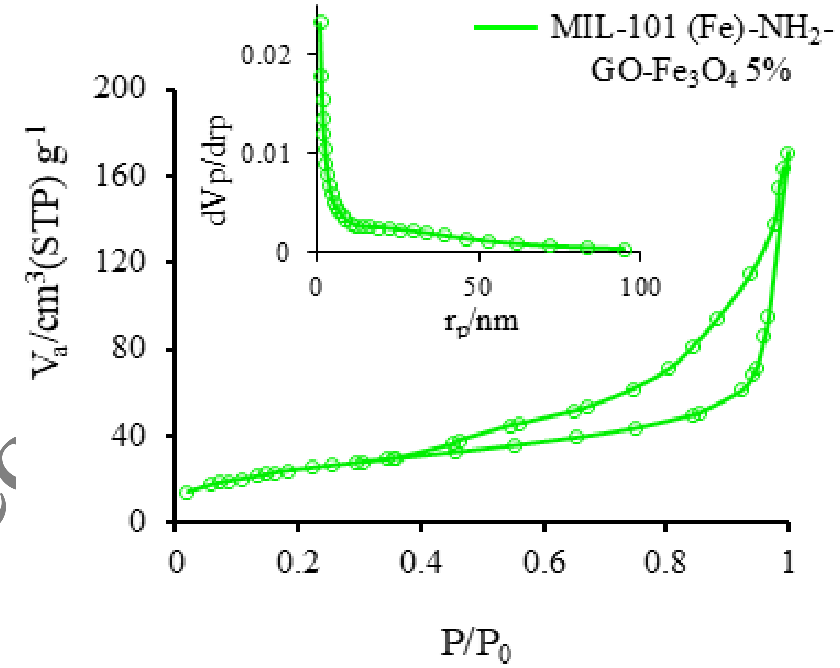
MIL-101 (Fe)-NH2-GO-Fe3O4 5%
Va/cm3(STP) g-1
200
160
120
80
40
0
0
0.2
0.4
0.6
0.8
1
P/P0
dVp/drp
0.02
0.01
0
0
50
100
rp/nm

(d)

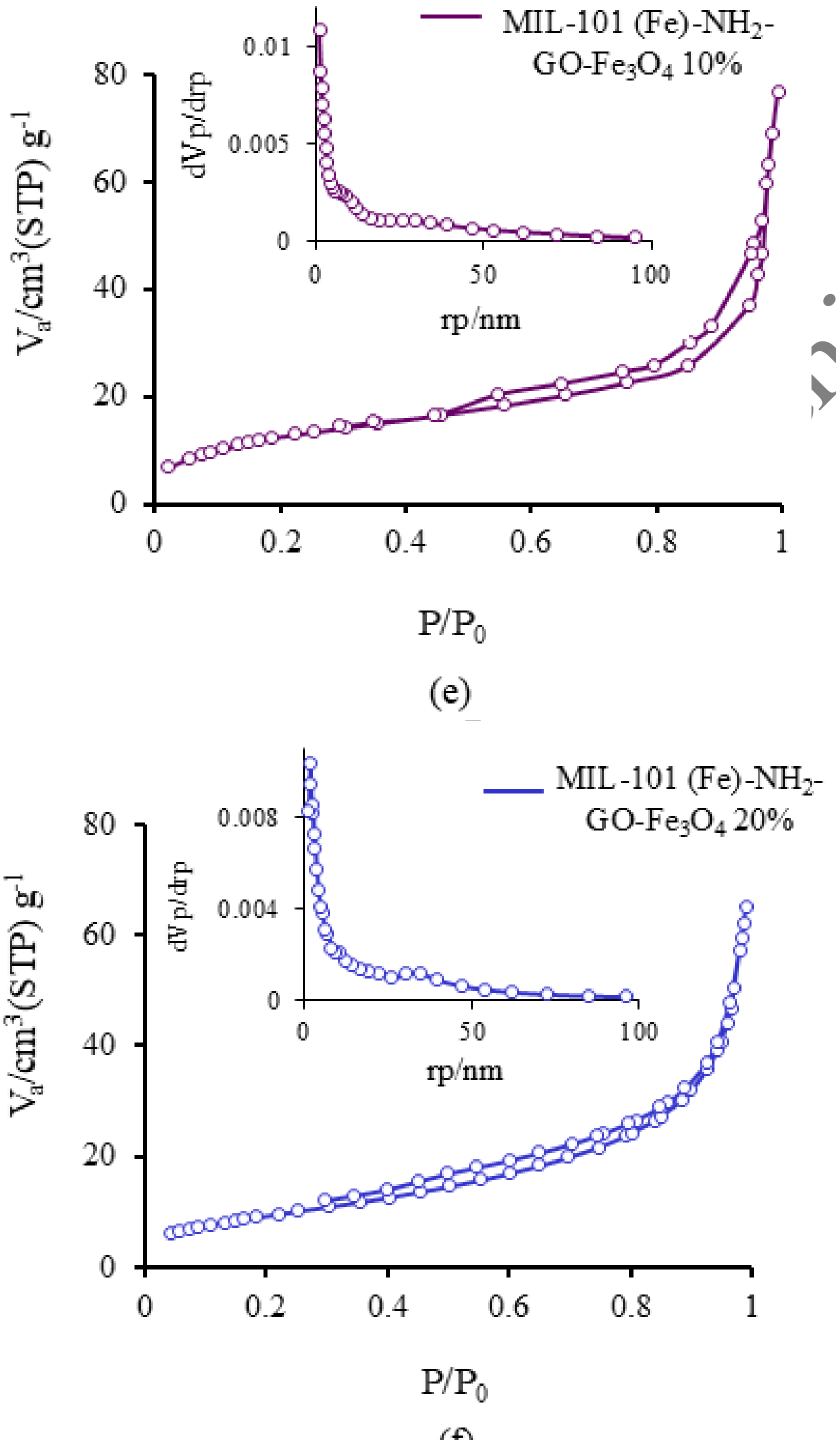
MIL-101 (Fe)-NH$_2$-GO-Fe$_3$O$_4$ 10%
V$_a$/cm^3(STP) g^{-1}
80
60
40
20
0
0
0.2
0.4
0.6
0.8
1
P/P$_0$
dVp/drp
0.01
0.005
0
0
50
100
rp/nm
MIL-101 (Fe)-NH$_2$-GO-Fe$_3$O$_4$ 20%
V$_a$/cm^3(STP) g^{-1}
80
60
40
20
0
0
0.2
0.4
0.6
0.8
1
P/P$_0$
dVp/drp
0.008
0.004
0
0
50
100
rp/nm

(e)

(f)

Figure 6.

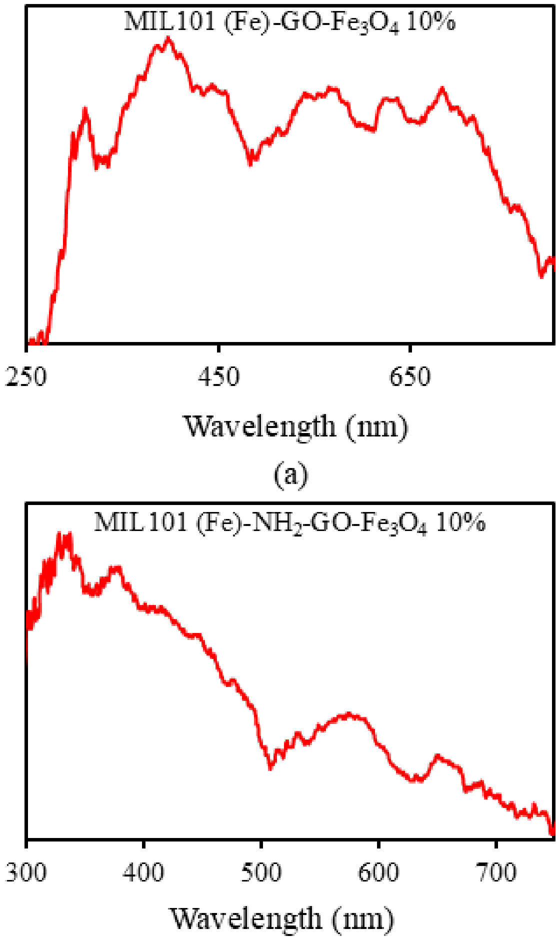

MIL101 (Fe)-GO-Fe$_3$O$_4$ 10%
250
450
650
Wavelength (nm)
(a)
MIL101 (Fe)-NH$_2$-GO-Fe$_3$O$_4$ 10%
300
400
500
600
700
Wavelength (nm)

(b)

Figure 7.

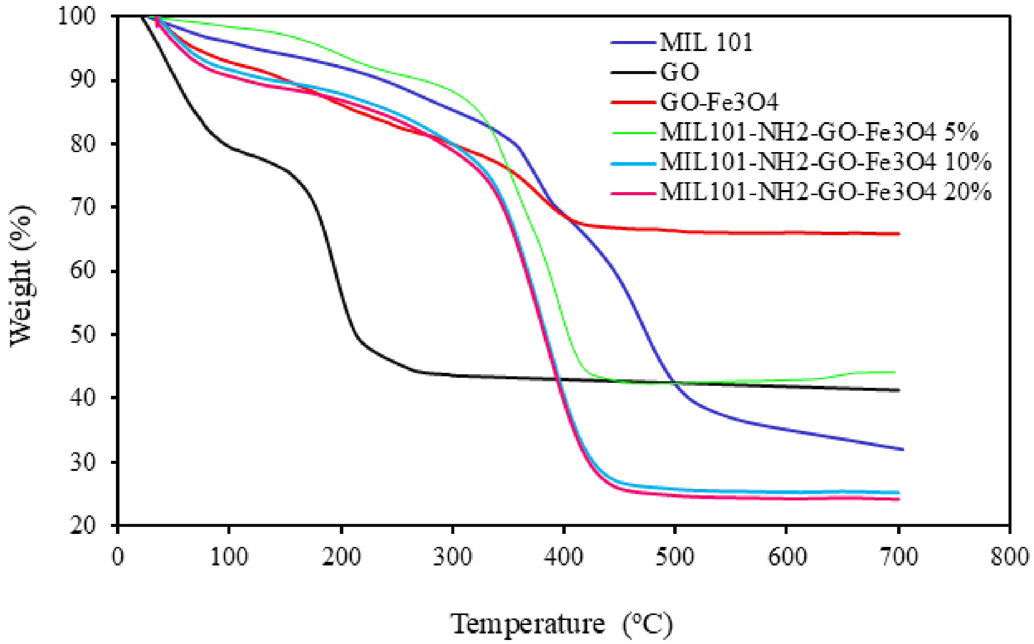
Weight (%)
100
90
80
70
60
50
40
30
20
0
100
200
300
400
500
600
700
800
Temperature (°C)
MIL 101
GO
GO-Fe3O4
MIL101-NH2-GO-Fe3O4 5%
MIL101-NH2-GO-Fe3O4 10%
MIL101-NH2-GO-Fe3O4 20%

Figure 8.

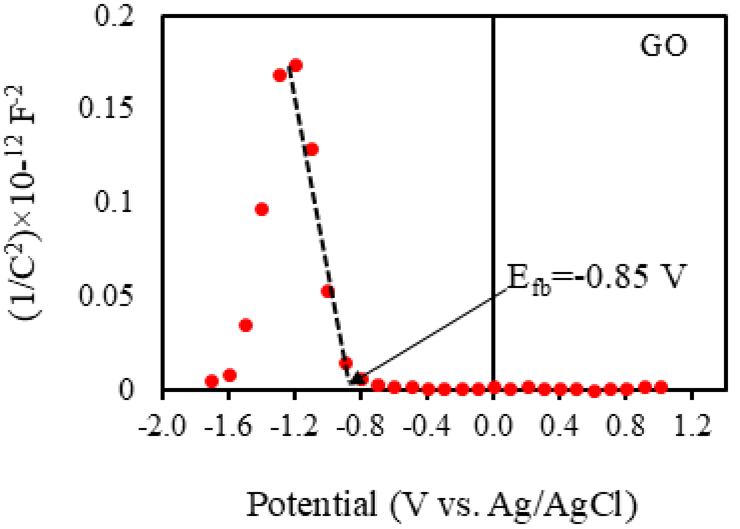
(1/C^2)×10^{-12} F^{-2}
0.2
0.15
0.1
0.05
0
-2.0
-1.6
-1.2
-0.8
-0.4
0.0
0.4
0.8
1.2
GO
E$_{fb}$=-0.85 V
Potential (V vs. Ag/AgCl)

(a)

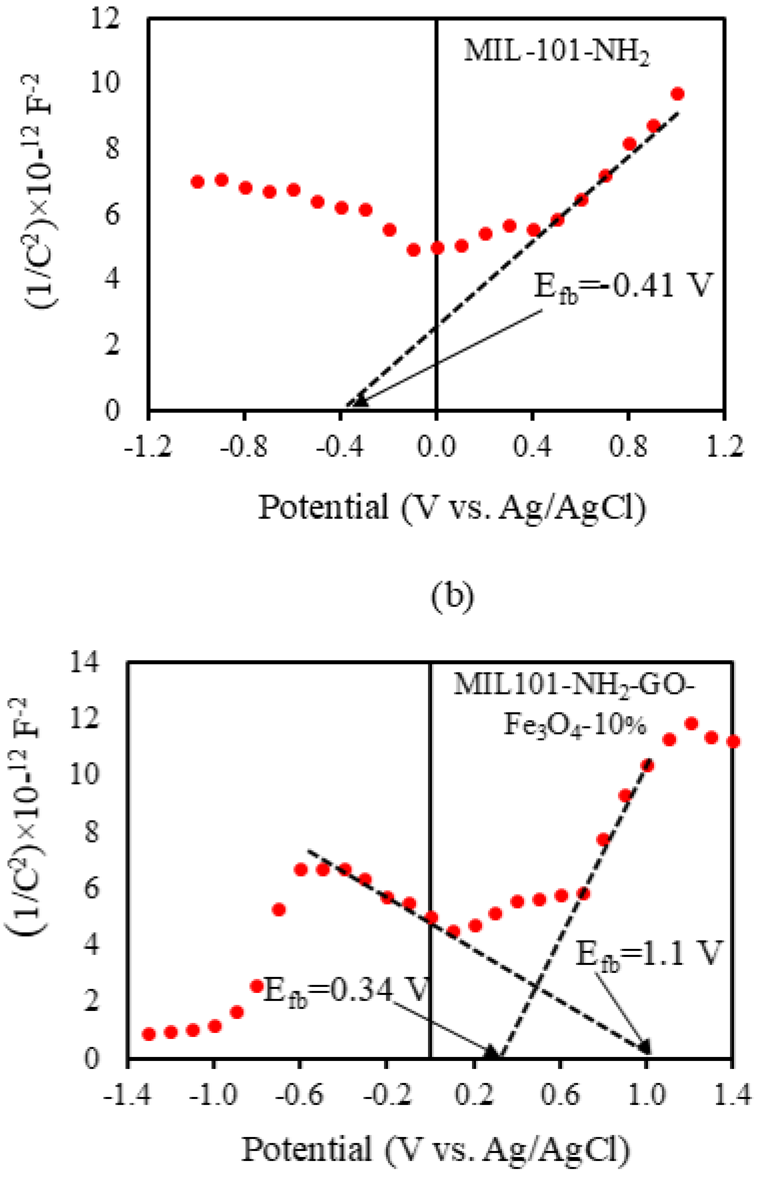
12
10
8
6
4
2
0
(1/C²)×10⁻¹² F⁻²
MIL-101-NH₂
E_fb=-0.41 V
-1.2
-0.8
-0.4
0.0
0.4
0.8
1.2
Potential (V vs. Ag/AgCl)
14
12
10
8
6
4
2
0
(1/C²)×10⁻¹² F⁻²
MIL101-NH₂-GO-
Fe₃O₄-10%
E_fb=1.1 V
E_fb=0.34 V
-1.4
-1.0
-0.6
-0.2
0.2
0.6
1.0
1.4
Potential (V vs. Ag/AgCl)

(b)

(c)

Figure 9.

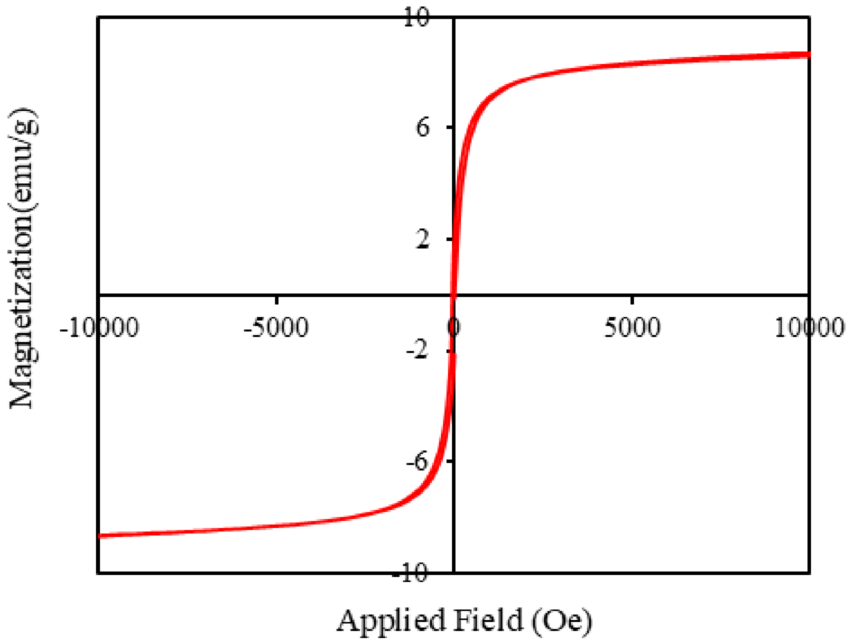

Figure 10.

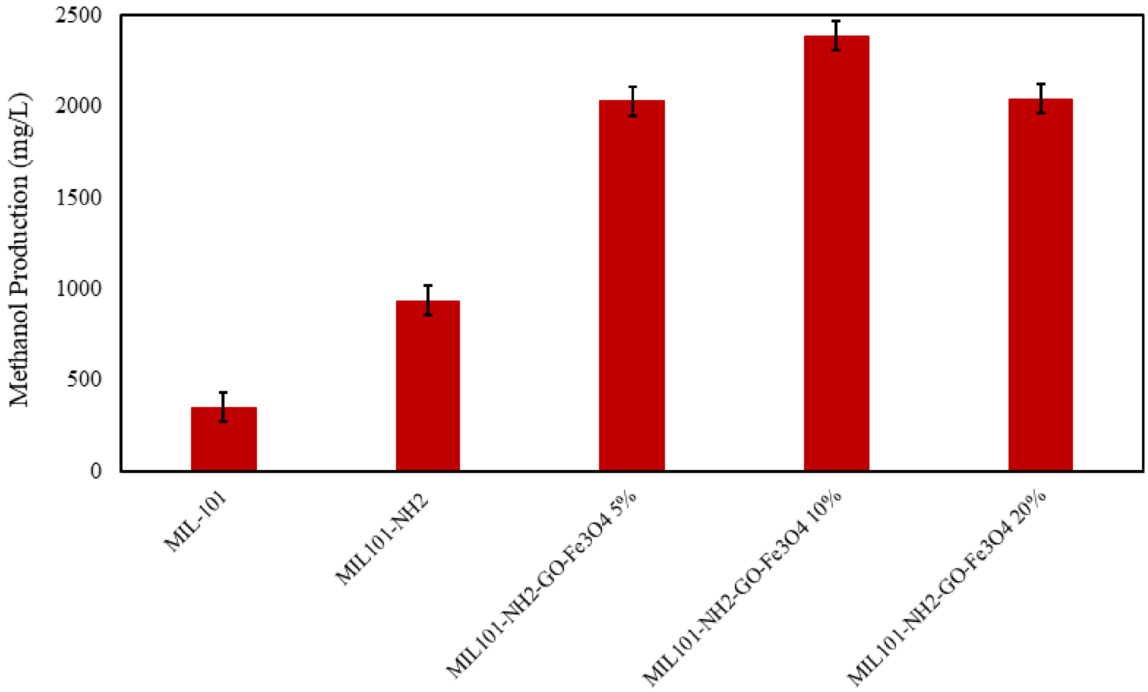

Figure 11.

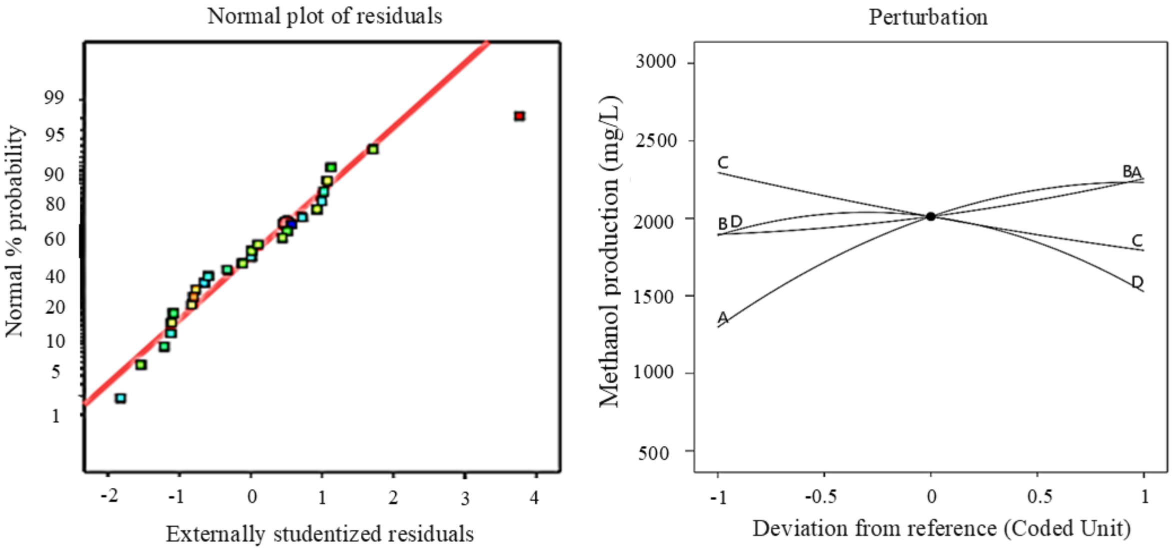
Normal plot of residuals
Normal % probability
99
95
90
80
60
40
20
10
5
1
-2
-1
0
1
2
3
4
Externally studentized residuals
Perturbation
Methanol production (mg/L)
3000
2500
2000
1500
1000
500
C
BA
B D
C
D
A
-1
-0.5
0
0.5
1
Deviation from reference (Coded Unit)

(a) (b)

Figure 12.

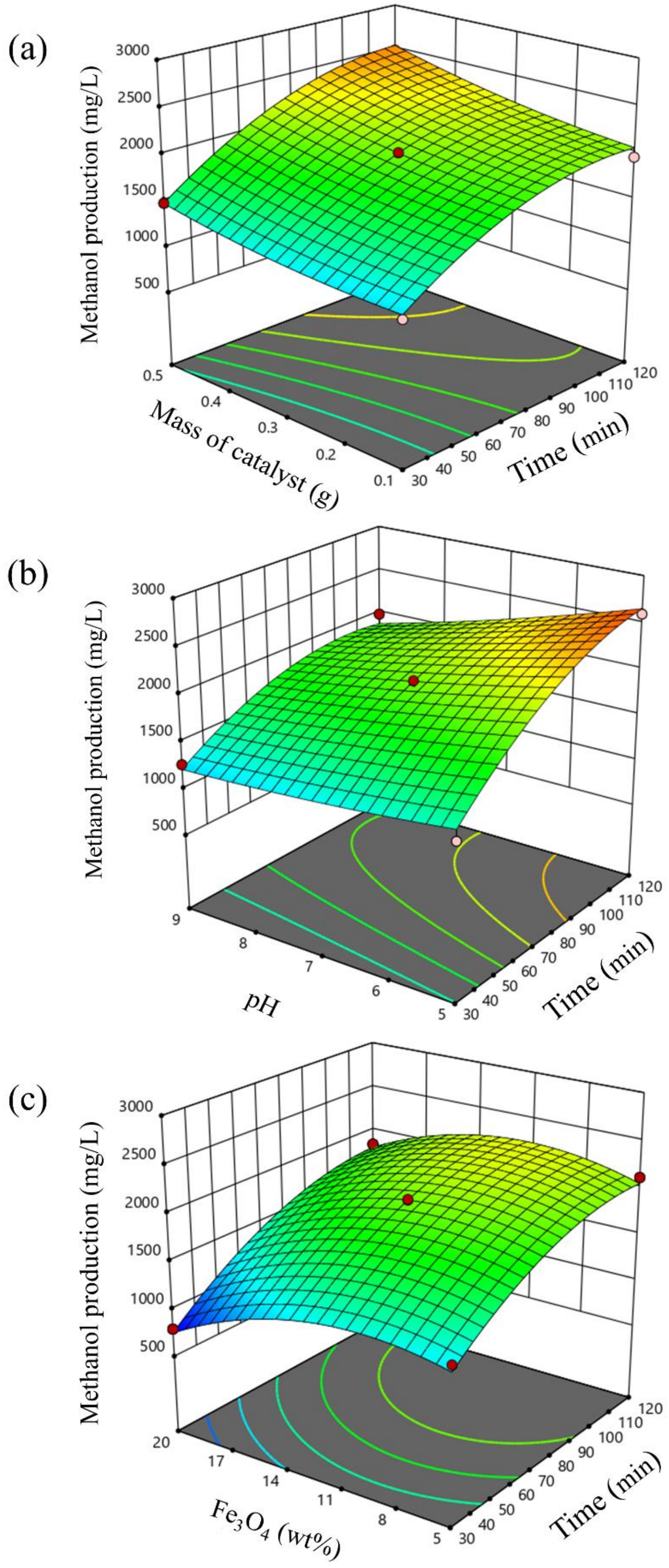
(a)
3000
2500
2000
1500
1000
500
Methanol production (mg/L)
0.5
0.4
0.3
0.2
0.1
Mass of catalyst (g)
30
40
50
60
70
80
90
100
110
120
Time (min)
(b)
3000
2500
2000
1500
1000
500
Methanol production (mg/L)
9
8
7
6
5
pH
30
40
50
60
70
80
90
100
110
120
Time (min)
(c)
3000
2500
2000
1500
1000
500
Methanol production (mg/L)
20
17
14
11
8
5
Fe$_3$O$_4$ (wt%)
30
40
50
60
70
80
90
100
110
120
Time (min)

Figure 13.

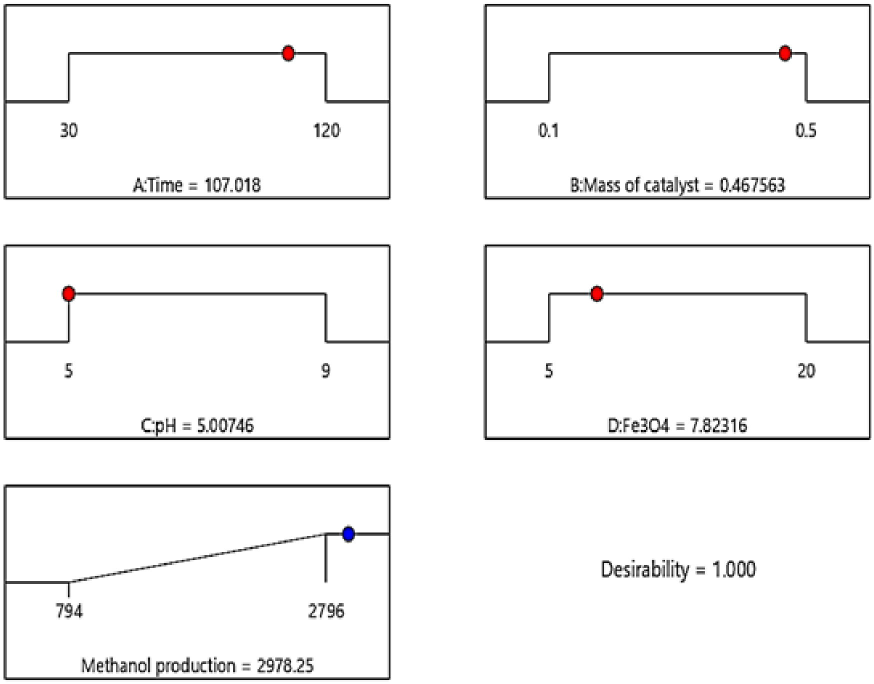
30
120
A:Time = 107.018
0.1
0.5
B:Mass of catalyst = 0.467563
5
9
C:pH = 5.00746
5
20
D:Fe3O4 = 7.82316
794
2796
Methanol production = 2978.25
Desirability = 1.000

Figure 14.

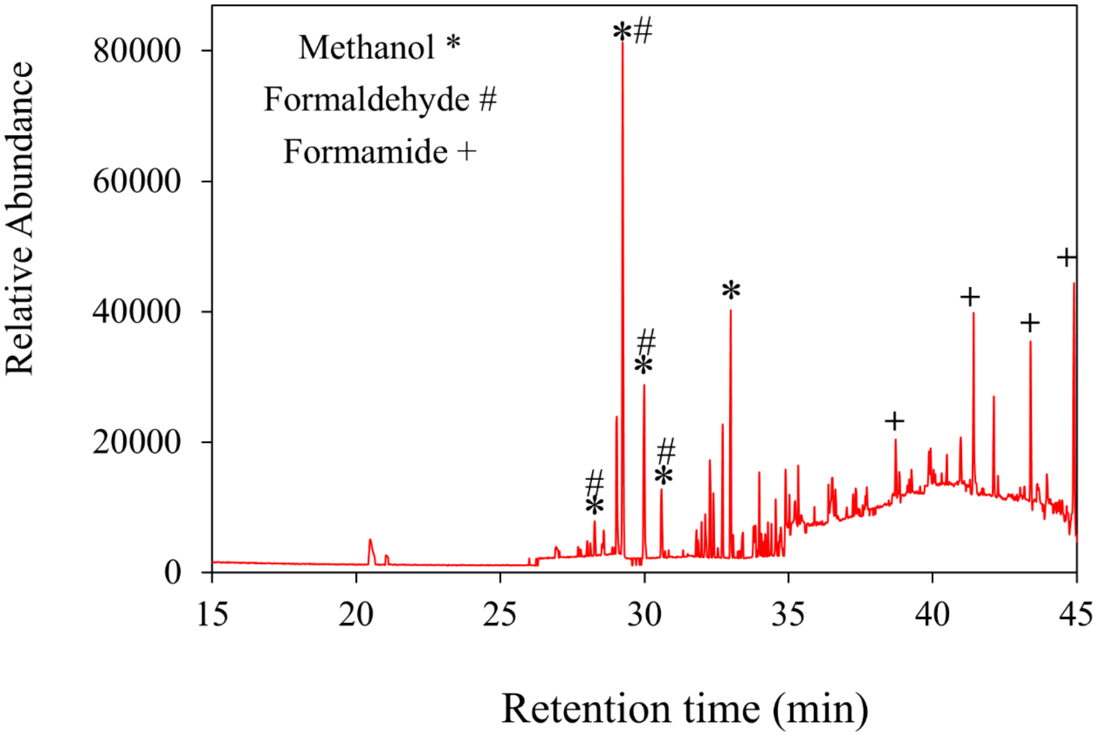
Methanol *
Formaldehyde #
Formamide +
Relative Abundance
80000
60000
40000
20000
0
15
20
25
30
35
40
45
Retention time (min)

Figure 15.

Tables

Table 1.

STD	RUN	Time (min)	Mass of catalyst (g)	pH	Fe_3O_4 (wt.%)	Methanol production (mg/L)
8	1	75	0.3	9	20	1413
7	2	75	0.3	5	20	1639
17	3	30	0.3	5	12.5	906
18	4	120	0.3	5	12.5	2597
5	5	75	0.3	5	5	1854
23	6	75	0.1	7	20	1532
14	7	75	0.5	5	12.5	2896
26	8	75	0.3	7	12.5	2001
2	9	120	0.1	7	12.5	1957
9	10	30	0.3	7	5	1305
6	11	75	0.3	9	5	981
12	12	120	0.3	7	20	1843
20	13	120	0.3	9	12.5	1987
19	14	30	0.3	9	12.5	1269
1	15	30	0.1	7	12.5	1194
4	16	120	0.5	7	12.5	2180
15	17	75	0.1	9	12.5	1677
22	18	75	0.5	7	5	2107
13	19	75	0.1	5	12.5	2282
27	20	75	0.3	7	12.5	2021
25	21	75	0.3	7	12.5	2013
24	22	75	0.5	7	20	1639
16	23	75	0.5	9	12.5	1997
21	24	75	0.1	7	5	1804
3	25	30	0.5	7	12.5	1485
10	26	120	0.3	7	5	2116
11	27	30	0.3	7	20	983

Table 2.

Photocatalyst	Band gap (eV)
MIL-GO-Fe-5%	1.90
MIL-GO-Fe-10%	1.82
MIL-GO-Fe-20%	1.87
MIL-NH_2-GO-Fe-10%	1.68
MIL-NH_2-GO-Fe-20%	1.76

Table 3.

Photocatalyst	a_s, BET ($m^2\ g^{-1}$)	Total pore volume ($cm^3\ g^{-1}$)	Mean pore diameter (nm)
MIL-101 (Fe)	342.92	0.32	3.74
GO	27.91	0.12	18.11
GO-Fe_3O_4	41.88	0.19	4.92
MIL-101 (Fe)-NH_2-GO-Fe_3O_4 5%	164.96	0.09	8.11
MIL-101 (Fe)-NH_2-GO-Fe_3O_4 10%	196.53	0.18	8.2
MIL-101 (Fe)-NH_2-GO-Fe_3O_4 20%	134.87	0.05	6.45

Table 4.

Source	Sum of squares	Degree of freedom	Mean square	F-value	P-value Prob >F	
Model	5.377E+06	14	3.841E+05	32.69	< 0.0001	Significant
A-Time	2.619E+06	1	2.619E+06	222.88	< 0.0001	
B-Mass of catalyst	3.881E+05	1	3.881E+05	33.03	< 0.0001	
C-pH	7.570E+05	1	7.570E+05	64.42	< 0.0001	
D-Fe_3O_4	3.968E+05	1	3.968E+05	33.77	< 0.0001	
AB	13456.00	1	13456.00	1.15	0.3056	
AC	76176.00	1	76176.00	6.48	0.0256	
AD	14161.00	1	14161.00	1.21	0.2938	
BC	21609.00	1	21609.00	1.84	0.2000	
BD	9604.00	1	9604.00	0.8173	0.3838	
CD	87025.00	1	87025.00	7.41	0.0186	
A^2	3.254E+05	1	3.254E+05	27.69	0.0002	
B^2	22533.33	1	22533.33	1.92	0.1913	
C^2	5808.00	1	5808.00	0.4943	0.4954	
D^2	4.913E+05	1	4.913E+05	41.81	< 0.0001	
Residual	1.410E+05	12	11750.39			
Lack of Fit	1.408E+05	10	14080.20	138.95	0.072	Not significant
Pure Error	202.67	2	101.33			
Cor Total	5.518E+06	26				

Leila Vafajoo’s Technical Information

Dr. Leila Vafajoo is an Associate Professor in the department of Chemical and Polymer Engineering at the Islamic Azad University, South Tehran Campus. Her academic journey includes the completion of her B.Sc. and M.Sc. Degrees at the Sharif University of Technology in 1994 and 1996, respectively. Subsequently, she earned her PhD from Amirkabir University of Technology (Tehran Polytechnique) on 2001. Dr. Vafajoo's extensive research portfolio is dedicated to the development, characterization, and physiochemical evaluation of adsorbents and catalysts designed for CO_2 capturing, as well as the treatment of industrial wastewater. Moreover, her scholarly pursuits encompass the mathematical modeling of chemical and environmental processes, alongside the innovation of lab-on-chip pollutant detection systems. Her multidisciplinary work significantly contributes to addressing of pressing global challenges of environmental sustainability and process engineering.

Mohammad Kazemeini's Technical Information

Mohammad Kazemeini received his B.E. degree from the Univ. of Minnesota at Minneapolis USA on 1984. Then he graduated with an M.S. degree from the Univ. of Virginia at Charlottesville, USA on 1986. Finally, he received his PhD degree from the Univ. of Illinois at Chicago, USA on 1990. Currently, he is a faculty member at the Chemical and Petroleum Engineering Dept. at the Sharif University holding a distinguished Professor Rank. His current research interests include; preparation, characterization and physiochemical evaluations as well as; mathematical modelling of chemical and physical kinetics of regular, Core-Shell and Magnetic catalysts. Furthermore, investigating Alumina, carbons (CNTs, Graphene Oxide and carbon Nano-Fibers), Zeolites and MOF supported catalysts and sorbents are being worked on. Moreover, designing and fabrication as well as investigating performance of microreactors and microfluidic systems applied to catalytic HDS and ODS (i.e.; Hydro- and Oxidative- Desulfurization) as well as; photocatalytic and catalytic API (i.e.; activated pharmaceutical ingredients) and organic as well as pharmaceutical pollutants removing materials are of close and recent interests.

Mohammad Shahriari Mazraeh Shahi's Technical Information

Mohammad Shahriari is progressing in Chemical Engineering. He earned his BSc degree from the Islamic Azad University (South Tehran Branch) in 2007 and a MSc degree from the Islamic Azad University (Shahrood Branch) in 2012. In 2016, he began his PhD studies at the Islamic Azad University (South Tehran Branch). His research focuses on developing photocatalyst composites from Metal-Organic Frameworks and Graphene Oxide. He studies how these catalysts can capture CO2 and convert it into fuel, utilizing a photoreactor under UVA conditions. This work demonstrates his commitment to addressing critical environmental challenges and contributes to the advancement of sustainable energy solutions